Probing dark matter with disappearing tracks at the LHC

Alexander Belyaev,[1,2,*] Stefan Prestel,[3,†] Felipe Rojas-Abatte,[2,‡] and Jose Zurita[4,5,§]

[1]*Rutherford Appleton Laboratory, Didcot OX11 0QX, United Kingdom*
[2]*University of Southampton, Southampton SO17 1BJ, United Kingdom*
[3]*Department of Astronomy and Theoretical Physics, Lund University, S-223 62 Lund, Sweden*
[4]*Institute for Nuclear Physics (IKP), Karlsruhe Institute of Technology, Hermann-von-Helmholtz-Platz 1, D-76344 Eggenstein-Leopoldshafen, Germany*
[5]*Institute for Theoretical Particle Physics (TTP), Karlsruhe Institute of Technology, Engesserstraße 7, D-76128 Karlsruhe, Germany*

(Received 5 October 2020; accepted 2 March 2021; published 10 May 2021)

Models where dark matter is a part of an electroweak multiplet feature charged particles with macroscopic lifetimes due to the charged-neutral mass split of the order of pion mass. At the Large Hadron Collider, the ATLAS and CMS experiments will identify these charged particles as disappearing tracks, since they decay into a massive invisible dark matter candidate and a very soft charged Standard-Model particle, which fails to pass the reconstruction requirements. While ATLAS and CMS have focused on the supersymmetric versions of these scenarios, we have performed here the reinterpretation of the latest ATLAS disappearing track search for a suite of dark matter multiplets with different spins and electroweak quantum numbers. More concretely, we consider the cases of the inert two Higgs doublet, minimal fermion dark matter and vector triplet dark matter models. Our procedure is validated by using the same wino and Higgsino benchmark models employed by the ATLAS Collaboration. We have found that with the disappearing track signature, one can probe a vast portion of the parameter space, well beyond the reach of prompt missing energy searches (notably monojets). We provide tables with the upper limits on the cross section and efficiencies in the lifetime—a dark matter mass plane for all the models under consideration, which can be used for an easy recast for similar classes of models. Moreover, we provide the recasting code employed here, as part of the public LLP recasting repository.

DOI: 10.1103/PhysRevD.103.095006

I. INTRODUCTION

The existence of Dark Matter (DM) has been established beyond any reasonable doubt by several independent cosmological observations. So far, only the gravitational interaction of DM has been experimentally confirmed (for a review, see [1]). However, its particle nature and properties are still to be elucidated.

If DM is light enough and interacts with Standard Model (SM) particles directly, or via some mediators with a strength beyond the gravitational one, its elusive nature can be detected or constrained in direct production at colliders. Therefore, the search for DM in high energy physics experiments became one of the primary goals of the LHC and future collider experiments (see, e.g., [2] and references therein).

The vanilla DM signal at colliders is the mono-X signature, where X stands for a SM object, such as jet, Higgs boson, Z, W, photon, top quark, etc. that recoils against the missing energy from the DM pair. This signature has limitations due to the large SM background from $Z \to \nu\nu$, as well as, typically, low signal cross section because of the requirement of large enough missing transverse momentum for the DM pair. In particular, if DM is part of a weak multiplet, and there are no light Z' resonances or other new particles playing the role of the mediators decaying into a DM pair (which could enhance DM mono-X signal), even the HL-LHC could probe DM mass only up to about 150–300 GeV, as shown, e.g., for the case of Higgsino DM in MSSM [3–6]. This limitation motivates us to go beyond the mono-X signature.

In this paper, we explore instead another signature, ubiquitous in beyond the Standard Model (BSM) with DM being part of a weak multiplet: *disappearing tracks*. In this scenario, the mass split between DM and its charged multiplet partner(s) can be generically small, in the

*a.belyaev@phys.soton.ac.uk
†stefan.prestel@thep.lu.se
‡F.Rojas-Abatte@soton.ac.uk
§jose.zurita@kit.edu

sub-GeV region, as we explain in what follows. If the DM sector consists of just an electroweak (EW) multiplet [7], then DM(D) and its charged partner(s) [$D^{+(+\ldots)}$] masses are degenerate at tree level, as required by the gauge invariance. This is clearly unacceptable from a cosmological point of view. However, this degeneracy is broken due to quantum corrections to D and D^+ masses from EW gauge bosons, which introduce the mass split $\Delta M \equiv M_{D^+} - M_D \propto \alpha_W M_W \sin^2(\theta_W/2)$, irrespectively of the specific quantum numbers (Y, T_3 and spin) with numerical value around 150–200 MeV. The mass split, which is nonzero at tree level in case of scalar DM (due to the quartic couplings with the SM Higgs field), should also be not too large due to perturbative unitarity constraints, which are particularly important for a large (of the order of 1 TeV) DM mass [see, e.g., the case of the inert two Higgs doublet model(i2HDM) [8]]. In an attempt to go beyond mono-X signature, one should note that theories with sub-GeV ΔM do not give any visible decays from D^+, even exploiting a boost from initial state radiation, a technique which can be useful for larger mass splits $\Delta M \gtrsim 2$ GeV [3].

Disappearing tracks occur at ΔM around 150–200 MeV, when D^+ becomes long lived[1] with a lifetime of the order of nanoseconds. In such a highly compressed scenario the $D^+ \to D\mathcal{Y}^+$ decay takes place, with $\mathcal{Y}^+$ being π^+ if $\Delta M > m_\pi$ or $\ell^+\nu$ if ΔM is below the pion mass. The $\mathcal{Y}^+$ are very soft and typically stopped by the magnetic field of the detector,[2] thus leaving a short-track (D^+) that "disappears" into missing transverse energy (D). This disappearing track (DT) signature which we explore in this paper is very powerful in probing DM scenarios which are compressed with $\Delta M \simeq m_\pi$.

ATLAS [13] and CMS [14] have actively searched for this signature, often driven by the supersymmetric scenarios of a "pure" Higgsino (weak doublet) and winos (weak triplets). The high potential of DT in probing DM masses in i2HDM model far beyond the monojet reach was explored in [8] for i2HDM model and in [15–17] for MSSM Higgsinos. Furthermore, the impact of disappearing tracks has also been studied for other models of dark matter and neutrino masses (see, e.g., [18–28]).

In this study, we present a simple and flexible recasting procedure based on the latest DT search by ATLAS [13], using publicly available information on experimental efficiencies and instrumental backgrounds. To do this, we first validate our approach by comparing our results for the MSSM wino and MSSM Higgsino scenarios used by ATLAS as benchmark models. Then, we apply our validated procedure to minimal models where DM is either a scalar, fermion, or vector. In order to facilitate the reinterpretation for other DM models, we provide our upper limits on cross sections and efficiencies in the lifetime-DM mass ($\tau - M_{\rm DM}$) plane in table format. In addition, the software developed for this reinterpretation procedure has been included in the public LLP Recasting Repository [29], together with a small event sample and the corresponding instructions. We expect this material to be useful to other groups for a straightforward reinterpretation of the ATLAS DT study.

The paper is structured as follows: in Sec. II, we set our DM model landscape which we use in our study for scalar, fermion and vector EW multiplets. In Sec. III, we briefly summarize the current status of disappearing track searches at the LHC and closely follow the study [13]. In this section, we define in details our recasting procedure and validate it against the published results for the wino AMSB scenario used as a benchmark by both ATLAS and CMS Collaborations. In Sec. IV, we present new results for the LHC limits for scalar, vector, and fermionic dark matter, highlight the impact of disappearing track searches for dark sector models beyond the default MSSM benchmarks and make our results available for a straightforward use by other groups. In Sec. V, we draw our conclusions. We reserve Appendix A for the definition of the collider objects employed in this work, Appendix B for a comparison between the MLM and CKKW-L matching schemes, and Appendix C for our cross section upper limits and efficiencies. More detailed information on cross section upper limits and efficiencies, including the one for single and pair $D^\pm$ production can be found in LLP Recasting Repository.

II. MODELS WITH DISAPPEARING TRACK SIGNATURES

In this section, we take a closer look into the viable scenarios of dark matter from weak multiplets with different spins and giving rise to disappearing track signatures.

In the case of simplest models with just one DM EW multiplet as an addition to the SM sector, the tree-level mass of all multiplet components is the same, as required by the gauge invariance. The charged and neutral components of the multiplet however receive different higher-order corrections. For multiplets with zero hypercharge, the mass of the charged particle(s) is always above $M_{\rm DM}$ [30–36][3] and the mass split $\Delta M \sim \alpha_W M_W \sin^2(\theta_W/2)$, which is of the order of the pion mass. This is a very important effect—it provides the neutral DM candidate and makes the charged particle from the multiplet naturally long-lived.

[1]There is an ongoing intense activity on studies for long-lived particles (LLPs) at the LHC. We refer the reader to [9] for a review of the theoretical motivations for LLPs and to [10] for an overview of the existing LHC searches.

[2]For a strategy to reconstruct the final state pion at ATLAS, see [11] and for electron-proton colliders, see [12].

[3]In the case of a nonzero hypercharge, negatively charged multiplet members could become lighter than DM mass due to the radiative corrections (depending on their charge and the mass), which eventually makes the model unacceptable.

Two important remarks are in order. First, in the case of the simplest model with a *scalar* DM multiplet, the scalar potential has to be supplemented with additional terms allowed by gauge invariance. This can provide a nonzero ΔM even at tree level. Second, we note that models with a nonzero hypercharge should be rescued from very high DM direct detection (DD) rates (otherwise, they would blatantly contradict the experimental results [37]) because of a nonvanishing DDZ DM interaction with Z boson. For fermionic DM,the minimal way to solve this problem is to introduce a Yukawa term, which splits Dirac DM into two Majorana components as we discuss below.

The benchmark models we have chosen are minimal consistent DM models with only a few parameters, represented by (a) the inert two Higgs doublet model (i2HDM) [38–41][4] for a spin zero DM multiplet; (b) the minimal fermion DM model (MFDM), where DM is a part of an EW doublet [42]); (c) the minimal spin-one isotriplet dark matter model featuring dark matter as a part of a vector triplet [43]. Further details on these models are given in the subsections below. We would like to stress that while all these models belong to the thermal dark matter class, our findings can be applied to more general scenarios, since our results are presented in a model-independent fashion, in terms of production rates in the lifetime-DM-mass plane.

For the sake of brevity, we denote Z_2-odd particles from DM multiplet as D particles and refer to the Z_2 symmetry as D parity. This notation will allow us to quickly switch between different models.

A. Inert 2-Higgs doublet model (i2HDM)

The i2HDM is a minimalistic extension of the SM with a second scalar doublet ϕ_D possessing the same quantum numbers as the SM Higgs doublet ϕ_s but with no direct coupling to fermions (the inert doublet). The scalar sector of the model is given by

$$\mathcal{L}_{i2\mathrm{HDM}} = |D_\mu \phi_s|^2 + |D_\mu \phi_D|^2 - V(\phi_s, \phi_D), \qquad (1)$$

where V is the potential with all scalar interactions compatible with the Z_2 symmetry,

$$\begin{aligned} V = & -m_1^2(\phi_s^\dagger \phi_s) - m_2^2(\phi_D^\dagger \phi_D) + \lambda_1(\phi_s^\dagger \phi_s)^2 + \lambda_2(\phi_D^\dagger \phi_D)^2 \\ & + \lambda_3(\phi_s^\dagger \phi_s)(\phi_D^\dagger \phi_D) + \lambda_4(\phi_D^\dagger \phi_s)(\phi_s^\dagger \phi_D) \\ & + \frac{\lambda_5}{2}[(\phi_s^\dagger \phi_D)^2 + (\phi_D^\dagger \phi_s)^2]. \end{aligned} \qquad (2)$$

In the unitary gauge, the SM doublet ϕ_s and the inert doublet ϕ_D take the form,

$$\phi_s = \frac{1}{\sqrt{2}}\begin{pmatrix} 0 \\ v + H \end{pmatrix}, \qquad \phi_D = \frac{1}{\sqrt{2}}\begin{pmatrix} \sqrt{2}D^+ \\ D + iD_2 \end{pmatrix}, \qquad (3)$$

where the first, SM-like doublet, acquires a vacuum expectation value v. After EW symmetry breaking (EWSB), the D parity is preserved by the absence of a vacuum expectation value for the second doublet, which forbids direct coupling of any single inert field to the SM fields and stabilizes the lightest inert boson. In addition to the SM-like scalar H, the model contains a charged D^+ and two neutral D and D_2 scalars from inert doublet. Following Ref. [8], we denote the two neutral inert scalar masses as $M_D < M_{D_2}$, so that we can identify D with the DM candidate.

The model can be conveniently described by a five-dimensional parameter space [8] using the following phenomenologically relevant variables:

$$\begin{aligned} & M_D, \qquad M_{D_2} > M_D, \qquad M_{D^+} > M_D, \\ & \lambda_2 > 0, \qquad \lambda_{345} > -2\sqrt{\lambda_1 \lambda_2}, \end{aligned} \qquad (4)$$

where M_D, M_{D_2} and M_{D^+} are, respectively, the masses of the two neutral and charged inert scalars, whereas $\lambda_{345} = \lambda_3 + \lambda_4 + \lambda_5$ is the coupling which governs the Higgs-DM interaction vertex HDD. Constraints on the parameter space have been comprehensively explored in the literature; see, e.g., [8,39–41,44–66].

The perturbativity requirement sets an upper limit on the absolute values of the $\lambda_3, \lambda_4, \lambda_5$ coupling, which is controlled by the value of the mass split between M_D, M_{D_2} and M_{D^+}. For $M_D \sim$ TeV, this mass split is limited to be below of about a GeV, which in turn provides the condition for LLPs. To summarize, we see that while in this model ΔM is nonzero at tree level, it is bounded by perturbativity to be relatively low, especially for large DM masses. Hence, a long-lived D^+ can naturally appear this model.

B. Minimal fermion dark matter model (MFDM)

In this model, DM is a fermion EW doublet with a nonzero hypercharge. This scenario is reminiscent of the Higgsino-bino system of the MSSM, and also of the singlet-doublet model. As previously discussed, one should implement a mechanism to suppress the DM scattering through a Z-boson exchange, in order to comply with the DD constraints from the XENON1T experiment [37].

The most minimal way to arrange this is to introduce a Yukawa interaction for the EW doublet with the SM Higgs doublet and an additional Majorana singlet fermion χ_s^0, resulting to the following Lagrangian [42]:

$$\begin{aligned} \mathcal{L}_{\mathrm{MFDM}} = & \mathcal{L}_{\mathrm{SM}} + \bar{\psi}(i\not{D} - m_\psi)\psi + \frac{1}{2}\bar{\chi_s^0}(i\not{\partial} - m_s)\chi_s^0 \\ & - (Y(\bar{\psi}\Phi\chi_s^0) + \mathrm{H.c.}), \end{aligned} \qquad (5)$$

[4]This model is known as the inert doublet model, often denoted as IDM, but here we use i2HDM acronym which, to our opinion, reflects better the nature of this model.

where Φ is the SM Higgs doublet. The DM $SU(2)$ vectorlike doublet with a hypercharge $Y = 1/2$ is defined as

$$\psi = \begin{pmatrix} \chi^+ \\ \frac{1}{\sqrt{2}}(\chi_1^0 + i\chi_2^0) \end{pmatrix}. \tag{6}$$

The last term of Eq. (5) is the aforementioned Yukawa interaction, which splits the neutral Dirac component of the doublet into two Majorana fermions with distinct mass eigenstates χ_1^0 and χ_2^0. We note that the previously studied doublet-singlet model [67–70] has four parameters including *two* Yukawa couplings, distinguishing left- and right-handed interactions of Higgs and DM doublets with a Dirac singlet, χ_s^0. In contrast, this model has only one Yukawa coupling involving the Majorana singlet, χ_s^0, and therefore, has only three free parameters: m_ψ, Y, and m_s.

The Yukawa interaction mixes χ_1^0 and χ_s^0 while χ^+ and χ_2^0 have the same mass m_ψ and remain degenerate at tree-level. This degeneracy is not essential, since χ_2^0 decay is driven by the $\chi_2^0 \to \chi_1^0 Z^{(*)}$ process. The three parameters m_ψ, Y, and m_s can be traded for three physical masses,

$$m_D, m_\psi \equiv m_{D^+} = m_{D_2}, \quad \text{and} \quad m_{D_3}, \tag{7}$$

corresponding to (D, D_2, D_3) mass bases of the neutral DM sector with the eventual mass order,

$$m_{D_3} > m_{D^+} = m_{D_2} > m_D. \tag{8}$$

This MFDM model, with singlet-doublet dark sector content, can be mapped onto a bino-Higgsino MSSM setup, in which all other SUSY particles (including winos) are decoupled.[5] In this model, DM does not interact with the Z boson, because χ_1^0 and χ_2^0 mass eigenstates are split, so the only relevant nonvanishing $Z\chi_1^0\chi_2^0$ vertex would not provide any DM direct detection rate at tree level. This allows us to avoid strong bounds from DM DD search experiments. At the same time, this model can naturally provide the right amount of DM abundance via effective $D - D_3$ or/and $D - D^+$ coannihilation or/and DM annihilation via Higgs boson exchange. The $D - D_3$ mixing angle θ and the mass split is defined by Yukawa coupling and m_ψ, m_s masses,

$$\tan 2\theta = \frac{2Yv}{m_\psi - m_s}. \tag{9}$$

One can see that if $m_s \gg m_\psi$, then D_3 decouples and ΔM becomes small, leaving the long-lived D^+ and dark matter D as the only experimentally accessible degrees of freedom in the spectrum. This limit has a direct one-to-one correspondence with the so-called "pure Higgsino" MSSM scenario, which is the benchmark model used by ATLAS in [71], and where the relic density is saturated for a dark matter mass of ∼1.1 TeV.

C. Minimal vector triplet dark matter model (VTDM)

The minimal vector triplet DM model supplements the SM with a new massive vector boson in the adjoint representation of $SU(2)_L$. The resulting Z_2 symmetric Lagrangian can be written as [43],

$$\begin{aligned} \mathcal{L}_{\text{VTDM}} = \mathcal{L}_{\text{SM}} &- \text{Tr}\{D_\mu V_\nu D^\mu V^\nu\} + \text{Tr}\{D_\mu V_\nu D^\nu V^\mu\} \\ &- \frac{g^2}{2}\text{Tr}\{[V_\mu, V_\nu][V^\mu, V^\nu]\} \\ &- ig\text{Tr}\{W_{\mu\nu}[V^\mu, V^\nu]\} + \tilde{M}^2\text{Tr}\{V_\nu V^\nu\} \\ &+ a(\Phi^\dagger\Phi)\text{Tr}\{V_\nu V^\nu\}, \end{aligned} \tag{10}$$

where $D_\mu = \partial_\mu - ig[W_\mu,]$ is the usual $SU(2)_L$ covariant derivative in the adjoint representation and V^μ represents the vector DM isotriplet. D parity prevents the new vector boson mixing with the SM gauge bosons after EWSB (which takes place exactly as in the SM). The physical mass of the new vector bosons, M_V, is given by

$$M_V^2 = \tilde{M}^2 + \frac{1}{2}av^2, \tag{11}$$

where $v \sim 246$ GeV is the usual SM Higgs vacuum expectation value.

In this model, the mass splitting between V and V^+ is induced only at the loop level. In a manner analogous to the fermionic case, the neutral and charged isotriplet components are degenerate at tree level, having the same mass M_V, as required by the gauge invariance. However, radiative EW corrections induce a ΔM split, making the neutral boson lighter than the charged ones. For $M_V \gg M_W, M_Z$, this split is given by [43]

$$\Delta M = \frac{5g_W^2(M_W - c_W^2 M_Z)}{32\pi} \approx 217.3 \text{ MeV}, \tag{12}$$

and a DM mass of the order of ∼3 TeV is necessary to achieve a relic abundance consistent with Planck constraints [72].

[5]The main difference between the MFDM and the MSSM (DM Higgsino case) is that in the latter the Yukawa coupling is the product of weak couplings and the $\tan\beta$ parameter, which is subject to nontrivial constraints from, e.g., flavor physics. We note, however, that this coupling affects the direct detection rates through Higgs exchange but is otherwise irrelevant for the collider phenomenology, as the production cross sections and the kinematic distributions (for the small mass split) are fully determined by the gauge couplings, spin, and weak charge of the EW multiplet.

D. The lifetime of charged LLPs and the effective W-pion mixing

The case of a small (below 1 GeV) split $\Delta M = M_{D^+} - M_D$ requires special consideration regarding the calculation of the D^+ width and hence, its lifetime. In particular, for ΔM just above the pion mass ($\Delta M \gtrsim m_{\pi^+} \simeq 140$ MeV), D^+ will dominantly decay into DM and π^+. This happens because when the $\Delta M \sim m_\pi$, the naive perturbative calculation of $D^+ \to DW^{+*} \to Du\bar{d}$ would underestimate the width by about 1 order of the magnitude and therefore would overestimate the lifetime of D^+ by the same factor (see, e.g., [8] for detailed discussion). For a proper evaluation of the lifetime (which is crucial for the LLP phenomenology), one should use the $W-\pi$ mixing, described by the nonperturbative term,

$$\mathcal{L}_{W\pi} = \frac{g f_\pi}{2\sqrt{2}} W^+_\mu \partial^\mu \pi^- + \text{H.c.} \tag{13}$$

with $f_\pi = 130$ MeV being the pion decay constant. This mixing leads to the effective $D^+D\pi^-$ interaction, which one can derive from the D^+DW^- gauge term by means of Eq. (13). The Feynman diagram for this interaction is presented in Fig. 1, which in terms of the effective Lagrangian for DM of spin 0, 1/2 and 1 in the momentum space reads as follows:

$$\mathcal{L}^{\text{i2HDM}}_{D^+D\pi^-} = -\frac{g^2 f_\pi}{4\sqrt{2}M_W^2}[(p_D - p_D^+)\cdot p_{\pi^-}]D^+D\pi^- + \text{H.c.} \tag{14}$$

$$\mathcal{L}^{\text{MFDM}}_{D^+D\pi^-} = -\frac{g^2 f_\pi}{4\sqrt{2}M_W^2}\cos(\theta_{DD_3}) p^\mu_{\pi^-} D^+\gamma^\mu D\pi^- + \text{H.c.} \tag{15}$$

$$\mathcal{L}^{\text{VDM}}_{D^+D\pi^-} = -\frac{g^2 f_\pi}{2\sqrt{2}M_W^2}[(p_D - p_{D^+})^\mu g^{\nu\rho} - p_D^\nu g^{\mu\rho} + p^\rho_{D^+} g^{\mu\nu}] p_{\pi^-\mu} D^+_\nu D_\rho \pi^- + \text{H.c.}, \tag{16}$$

where $\cos(\theta_{DD_3})$ stands for the cosine of the $D-D_3$ mixing angle for the case of MFDM model. It is worth stressing that the interactions for fermion DM can have a more general form, by including different left and right DM couplings. The archetypical example of such a model is the MSSM, where the relevant interactions have the form,

$$\mathcal{L}^{\text{MSSM}}_{D^+D\pi^-} = -\frac{g^2 f_\pi}{4\sqrt{2}M_W^2} p_{\pi^-\mu} D^+[g_L\gamma^\mu P_L + g_R\gamma^\mu P_R]D\pi^- + \text{H.c.}, \tag{17}$$

where g_L and g_R are left and right couplings defined by the specific chargino and neutralino mixings, while P_L and P_R are the respective left- and right-handed projectors.

The minimal DM models discussed above together with the effective $D^+D\pi^-$ interactions given by the above Eqs. (14)–(16) are implemented into CalcHEP [73] using the LanHEP package [74–76], and allows us to effectively and accurately carry out the detailed study of the LLP phenomenology of EW DM with different spins, which is presented in the following sections. We have made these models publicly available at High Energy Physics Model Database (HEPMDB) [77].

III. VALIDATION OF THE DISAPPEARING TRACK SEARCH

A. Existing experimental studies

Here, we will review the most salient features of the ATLAS disappearing track analysis [13]. The relevant signal process for the models under study is the pair production of new fields are $pp \to D^\pm D$ and $pp \to D^+D^-$. To trigger events, one can use the initial-state radiation-induced monojet signature, since disappearing tracks contribute to the missing transverse energy (MET) if the lifetime of $D^\pm$ is not too large, such that the $D^\pm$ particles do not enter the hadron calorimeter. One should require MET as low as possible for this triggering to keep as many signal event as possible. That is why $pp \to \chi_1^\pm\chi_1^0 j$ and $pp \to \chi_1^+\chi_1^- j$ SUSY processes were the subject of the particular ATLAS study mentioned above. Exemplary Feynman diagrams are shown in Fig. 2. The event preselection is qualitatively simple and requires the

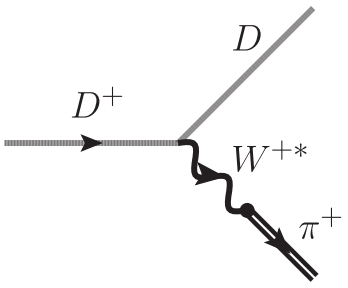

FIG. 1. Feynman diagram depicting the effective $D^+D\pi^-$ interaction from $W-\pi$ mixing.

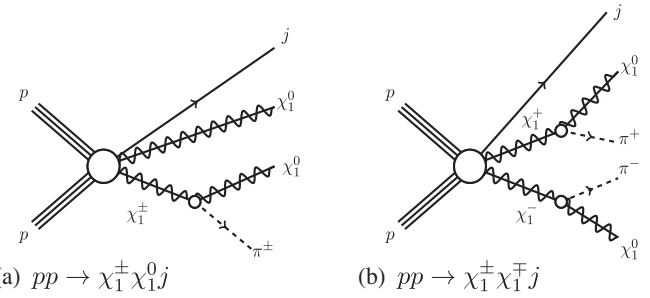

FIG. 2. Example diagrams of the signal process used in the analysis.

presence of at least one isolated *tracklet*, a large amount of missing transverse energy E_T^{miss}, and at least a high p_T jet. A tracklet is a special type of shorter track introduced specifically for this search and serves as a proxy for the disappearing track signal. Trackets are reconstructed using information from the ATLAS pixel layers of the inner detector, while all other collider objects (jets, muons, electrons) use standard definitions. For completeness, we specify the necessary quality cuts on the objects in Appendix A.

After the preselection stage, two more steps follow. First, the *event selection* takes place, with the goal of isolating the signal from the SM backgrounds. Later, a *tracklet selection* is carried out. Only good quality tracklets are selected. The ATLAS Collaboration has provided in their auxiliary material in HEPDATA [78] information to reinterpret (recast) this study. Its proper use requires us also to define generator level instances of both the *event* and *tracklet* selections, which are obviously based on reconstructed objects. Using public information, one can account with a reasonable precision for detector effects for standard objects such as jets, muons, electrons, etc. However, the vital ingredient here is how the parton-level chargino becomes a tracklet (reconstructed-level object). The information at the generator level provides the recaster a sanity check of the different selections, unfolding reconstruction effects. The combination of the reconstructed and generator level information allows us to define a model-independent probability for a parton level chargino to become a tracklet. Our goals here are to first validate the reported probabilities using the same signal model (and parameter points) as in the ATLAS study and second to apply these validated efficiencies to a wide class of models under study.

1. The event selection stage

After the reconstruction stage, event are selected by applying the following requirements:

(1) At least one jet with $P_T > 140$ GeV.
(2) $E_T^{\text{miss}} > 140$ GeV, the *high* E_T^{miss} region, to discriminate the signal from the SM process.
(3) The difference in azimuthal angle $(\Delta\phi)$ between the missing transverse momentum and each of up to four highest-P_T jets with $P_T > 50$ GeV is required to be larger than 1.0.
(4) Candidates events are required to have no electron and no muon (lepton veto).

At the generator level stage, the event selection follows the same criteria, except that the object definition is slightly different. The generator level missing transverse energy (dubbed "offline missing energy" by ATLAS) is defined as the vector sum of the transverse momentum of neutrinos, neutralinos, and charginos (the tracklet p_T is not used).[6]

[6]Note that the vector sum of the transverse momentum of neutrinos, neutralinos, and charginos is done at the parton level before charginos decay.

Generator level jets are defined using the anti-kt algorithm with a radius parameter of 0.4 over all particles except for muons, neutrinos, neutralinos, and charginos with $c\tau$ above 10 mm. Defining

(i) N as the total number of chargino events,
(ii) N_{gl} as the number of chargino events passing the generator-level kinematic selection,
(iii) N_{es} as the number of chargino events passing the event selection,

the event acceptance E_A and event efficiency E_E are given by

$$E_A = \frac{N_{\text{gl}}}{N}, \qquad E_E = \frac{N_{\text{es}}}{N_{\text{gl}}}. \tag{18}$$

We stress that the model dependent quantities E_E and E_A can be computed directly from Monte Carlo simulation, as they do only involve standard reconstructed objects (no requirement on tracklets).

It is important to note that E_E could be larger than one, because an event could be failing the generator-level cuts while passing the reconstructed level selection due to object resolutions. As a concrete example, a signal event could have a leading jet of $p_T = 135$ GeV at a parton level and $p_T = 145$ GeV at a reconstructed level. Such an event would not be included in N_{gl}, but would be part of N_{es}.

2. The tracklet selection stage

After the event selection stage, the ATLAS Collaboration applies a series of requisites to the tracklets, in order to reduce the expected background. Due to the inherent nature of the tracklet as a reconstructed object, we can not reproduce this part of the analysis. Hence, we need to resort to the public information provided by ATLAS in the auxiliary material [78] in order to validate our analysis. The tracklet selection of ATLAS requests

(i) *Isolation and P_T requirement*
  – The separation ΔR between the candidate tracklet and any jet with $P_T > 50$ GeV must be greater than 0.4.
  – The candidate tracklet must have $P_T > 20$.
  – The candidate tracklet must be isolated. A track or tracklet is defined as isolated when the sum of the transverse momenta of all standard ID tracks with $p_T > 1$ GeV and $|z_0 \sin(\theta)| < 3.0$ mm in a cone of $\Delta R = 0.4$ around the track or tracklet, not including the p_T of the candidate track or tracklet, divided by the track or tracklet p_T, is small: $p_T^{\text{cone40}}/p_T < 0.04$.
  – The P_T of the tracklet must be the highest among isolated tracks and tracklets in the event.
(ii) *Geometrical acceptance*
  – The tracklet must satisfy $0.1 < |\eta| < 1.9$.

(iii) *Quality requirements*
- The tracklet is required to have hits on all four pixel layers.
- The number of pixel holes, defined as missing hits on layers where at least one is expected given the detector geometry and conditions, must be zero.
- The number of low-quality hits associated with the tracklet must be zero.
- Tracklets must satisfy requirements on the significance of the transverse impact parameter, d_0, $|d_0|/\sigma(d_0) < 2$ [where $\sigma(d_0)$ is the uncertainty in the d_0 measurement], and $|z_0 \sin(\theta)| < 0.5$ mm. The χ^2 probability of the fit is required to be larger than 10%.

(iv) *Disappearance condition*
- The number of SCT hits associated with the tracklet must be zero.

This selection contains criteria that are impossible to employ in an independent analysis. Thus, in contrast, the simple generator-level selection is defined as follows:

(i) $P_T > 20$ GeV.
(ii) $0.1 < |\eta| < 1.9$.
(iii) 122.5 mm $< R <$ 295 mm, where R is the decay position defined as the cylindrical radius relative to the origin. These two values correspond to the location of the fourth pixel layer and the first layer of the semiconductor tracker (SCT), respectively.
(iv) $\Delta R > 0.4$ between the chargino and each of the up to four highest-P_T jets with $P_T > 50$ GeV.

In total analogy with the "event selection" stage, we will introduce the following quantities:

(i) $n_{\rm gl}$ as the number of charginos that pass the generator-level tracklet selection in events that pass the event selection,
(ii) $n_{\rm rec}$ as the number of reconstructed events where at least 1 chargino is identified,
(iii) n total number of charginos in events that pass the event selection.

From these, the tracklet acceptance T_A and tracklet efficiency T_E are computed as

$$T_A = \frac{n_{\rm gl}}{n}, \qquad T_E = \frac{n_{\rm rec}}{n_{\rm gl}}. \tag{19}$$

In order to calculate $n_{\rm rec}$, we need to use the $T_A T_E$ efficiency heatmap provided by ATLAS in the auxiliary material [78], where a given η and radial decay distance r, and the product $T_A T_E$ is provided. As a final ingredient, the ATLAS Collaboration provides the tracklet p_T efficiency P, which is the probability that a tracklet passing the acceptance condition will have $p_T > 100$ GeV.[7]

With all the ingredients at hand, we can then explicitly write down the probability for a parton level event with N charginos to have at least one reconstructed tracklet, which is given by

$$1 - p(N,0) = E_E E_A (1 - (1 - T_A T_E P)^N), \tag{20}$$

where $p(i,j)$ is the probability that a parton level event with i charginos yields j reconstructed tracklets in the final state. This result coincides exactly with that quoted by ATLAS in footnote 5 of their paper and thus, provides an additional sanity check to our understanding of the analysis description.

In order to compute $n_{\rm rec}$ from our parton level events, we proceed as follows. We consider that in the ith event, we have at most two charginos, which have a value of $T_A T_E$ given by the ATLAS heatmap which for short we call ϵ_1 and ϵ_2. Hence, for this event, we have

$$p(1,1) = \epsilon_1, \qquad p(2,1) = \epsilon_1(1-\epsilon_2) + \epsilon_2(1-\epsilon_1),$$
$$p(2,2) = \epsilon_1 \epsilon_2, \tag{21}$$

where to keep a simple notation, we will omit an event dependent subscript "i" on each $p(a,b)$ function. Summing over all events, we have that $n_{\rm rec} = \sum (p(1,1) + p(2,1) + p(2,2))$, allowing us to compute, for a given point in the $(m_\chi - c\tau)$ plane, T_A and T_E. One should note that the ATLAS analysis has imposed the condition to keep only the hardest tracklet in the event. We have adopted this approach in our analysis; however, the probability that there will be two tracklets in the event is quite low. The fraction of such events is below a percent for this particular study—one can estimate this from Eq. (21), given that ϵ_1 and ϵ_2 are below 0.01 (as quantified below). On the other hand, in the future analysis at high luminosity regime with higher pileup (and, respectively, higher background), taking into account events with two tracklets could be instrumental to improve LHC sensitivity to the new physics with DT signatures.

B. Validation in the AMSB scenario

The ATLAS study uses as a benchmark the minimal anomaly mediated supersymmetry breaking (AMSB) scenario [79,80], where $\tan\beta = 5$, the universal scalar mass is set to $m_0 = 5$ TeV, and the sign of the Higgsino mass term set to be positive. We performed a scan of chargino masses between 91 GeV and 700 GeV and lifetimes between 10^{-2} and 10 ns. Our signal simulation uses up to one additional parton in the matrix element with CalcHEP 3.7.5 [73], using the AMSB implementation (http://hepmdb.soton.ac.uk/hepmdb:1013.0145) for parton level events, using PYTHIA v8.2.44 [81] for parton shower and hadronization, and finally, using DELPHES 3.4.1 [82] to simulate the detector effects, employing the default ATLAS card. We employed the `NNPDF23_lo_as_0130_qed` parton distribution functions [83], a QCD scale equal to the invariant mass of the pair of winos was used for the calculation of the cross section at leading order (LO), and corrections

[7]In the ATLAS study, this quantity is indistinctively called P and T_P. We thank Ryu Sawada for clarifying the confusion.

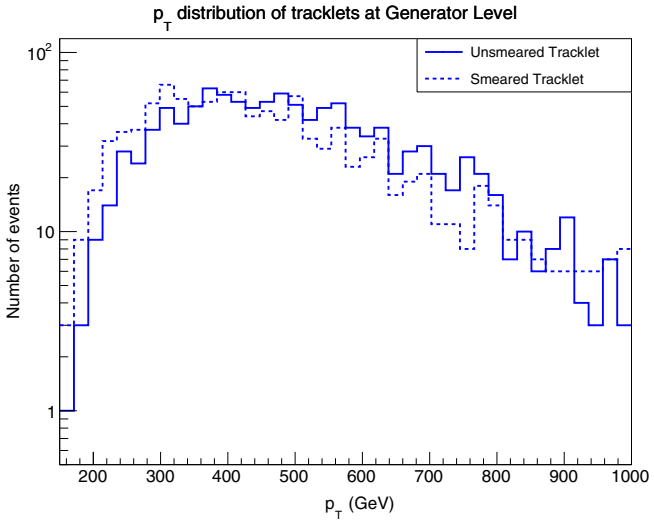

FIG. 3. Transverse momenta distribution p_T of the chargino at the truth level (solid line) and smeared (dashed line) using a random scaling with 15% amplitude.

at next-to-leading order (NLO) in the strong coupling constant were obtained using Prospino2 [84].

The Collaboration has chosen three benchmark points to showcase the efficiencies and acceptances discussed in the previous subsection, making public the SLHA cards for each of these points. We have found this to be a good practice and highly useful to validate our event generation pipeline, and we believe that in the spirit of the recommendations from the reinterpretation forum [85], signal cards should be made public whenever possible. There are two effects on the signal that we would like to discuss in more detail in the next paragraph, namely the impact of smearing the parton-level chargino track and the effect of combining the signal fixed-order calculation with the parton shower event generator.

To quantify the effects of the track smearing, we have implemented the ATLAS tracker transverse momentum resolution given by Gaussian smearing with $\sigma_{p_T}/p_T = 0.05\% p_T/\text{GeV} \bigoplus 1\%$ [86] and have found that it has a small impact in the p_T distribution of the chargino, as displayed in Fig. 3. We have checked explicitly that the difference between the selected number of events at generator level with and without smearing is less than 2%.

Since both event and tracklet selection put strong constraints on jets, as well as include nontrivial cuts on correlations between jets and electroweak objects, multijet activity in the signal process has to be carefully modeled. Thus, multijet merged calculations are mandatory to obtain a tree-level accurate description of radiative spectra, and for minimizing the impact of (parton shower) approximations on the signal description. However, multijet merged calculations have historically been developed and tested for SM background processes. This means that the choices made in specific merging schemes do not necessarily guarantee an accurate modelling also for very high energy BSM signals. For example, typical values of renormalization and factorization scales for SM processes are of the order of the electroweak scale. Since the factorization scale determines the amount of additional initial-state radiation, the phase space for additional QCD radiation tends to be moderately small for SM processes. Thus, the impact of many-parton (i.e., many-jet) configurations on inclusive observables is moderate or absent. Hence, the differences between merging schemes are small, leading to relatively robust predictions of backgrounds.

The same level of robustness is not guaranteed in the prediction of multijet sensitive signals. Differences between different merging schemes appears at higher jet multiplicity:

(i) Differences arise due to the treatment of phase-space points do not allow the interpretation as being produced by a sequence of QCD emissions with decreasing hardness [87–90].
(ii) Methods to assign factorization scales for many-jet events may differ. In particular, factorization scales are set on the basis of jet clustering in CKKW-inspired approaches [91,92], but not in the MLM method [93,94].
(iii) Various schemes to assign dynamic renormalization scales exist [90–92,95]. In MLM, renormalization scales are set using the nodal jet separation values of the kt algorithm, while the renormalization scale setting procedure in CKKW-L is identical to the scale setting procedure of the parton shower model. Using the kt-algorithm jet separation, values can potentially result in small renormalizaton scales for events that do not allow an interpretation as ordered sequence of QCD emissions. This leads to artificially large values of the running (strong) coupling, as, e.g., discussed in [90,96].

The general expectation is that if more phase-space is available for many-jet configurations, then different merging schemes will give a wider spread of predictions. For the signal process at hand, the phase space available for (initial-state) QCD radiation is large, due to the high energy required to produce the signal. Thus, the impact of higher-multiplicity calculations is not necessarily small, and a robust prediction of the signal is not guaranteed [97]. An estimate of the uncertainty due to the choice of matching scheme becomes mandatory in this case. We use two different multijet merging schemes to estimate the size of this uncertainty: MLM jet matching [94] and CKKW-L multijet merging [87,91].[8] As shown in detail in Appendix B, distributions for leading

[8]This study lead to the identification of several critical errors in both the MLM and CKKW-L implementation in PYTHIA, (a) regarding the definition of processes with BSM resonance chains in the CKKW-L scheme and (b) in the event rejection procedure, which is necessary to produce no-emission probabilities, for both merging schemes. The necessary corrections have been included in PYTHIA 8.245.

TABLE I. Event and tracklet acceptances and efficiencies (see main text for definitions) for some signal models, as an example. Our results are shown within the parenthesis. The final column Δ show the ratio between the ATLAS values and our own. The overall error is around 20%, which is acceptable for a simplistic parton level simulation of the signal. We also note that the bulk of the difference originates from the "tracklet" stage.

Signal		Event		Tracklet		
$m_\chi^\pm$ (GeV)	τ (ns)	E_A	E_E	T_A	T_E	Δ
400	0.2	0.09 (0.09)	1.03 (1.03)	0.07 (0.08)	0.47 (0.44)	1.211
600	0.2	0.12 (0.10)	1.05 (1.03)	0.05 (0.06)	0.48 (0.44)	1.289
600	1.0	0.11 (0.10)	1.03 (1.03)	0.20 (0.22)	0.47 (0.43)	1.169

jet transverse momentum and for transverse momentum of $\chi^+\chi^-$ pair indeed differ between two merging schemes.

The CKKW-L scheme yields a smooth, physical p_T distribution irrespective of the merging scale, while the event rejection in MLM jet matching induces visible matching artifacts in the transition region when the merging scale is not "tuned" so that the prediction recovers a target baseline. In the case of pair D^+D^- production, the merging scale value has potentially large uncertainty, since values that might be considered reasonable range from the transverse momentum of the D^+D^- pair (of the order of 100 GeV) to the invariant mass of D^+D^- pair (of the order of TeV). Therefore, for a proper handling of the transition region, we have adopted the CKKW-L scheme throughout the whole article. We use MLM scheme as a cross-check to assess if our conclusions depend heavily on the (highly scheme-dependent) dynamics of regions with moderate jet separation.

We reproduce the information on the acceptances and efficiencies in Table I, together with our own results which are displayed in parenthesis. We also present the ratio of the product $E_A E_E T_A T_E$ between ATLAS and our simulation. We see that we err by up to 20%, which is acceptable for a simplistic parton level simulation of the signal. We also see that our rate is lower than the corresponding one from ATLAS, and hence, in these particular points, our simulation gives a conservative estimate of the ATLAS result.

Since the ATLAS Collaboration provided 2D binned results for the product $T_A T_E$ in the $(m_{\chi_1^\pm} - c\tau)$ plane, we thus show our own results and the ratio between those and the reported ATLAS values in Fig. 4. We thus confirm that in most of the parameter space, we are within a 20% error on the efficiency, while these values degrade when going to the edges of the scanned space.

In order to obtain exclusion limits that we can compare with the published ATLAS results, we still need to discuss the background events. The dominant backgrounds for the disappearing track signature are mostly of instrumental nature and hence, cannot be simulated with an event generator, but are rather obtained from the experimental data itself. In fact, the leading background after the tracklet selection is given by fake tracklets, namely, those coming from random hits of particles in the pixel layers. We need then to rely on the published p_T distribution of the

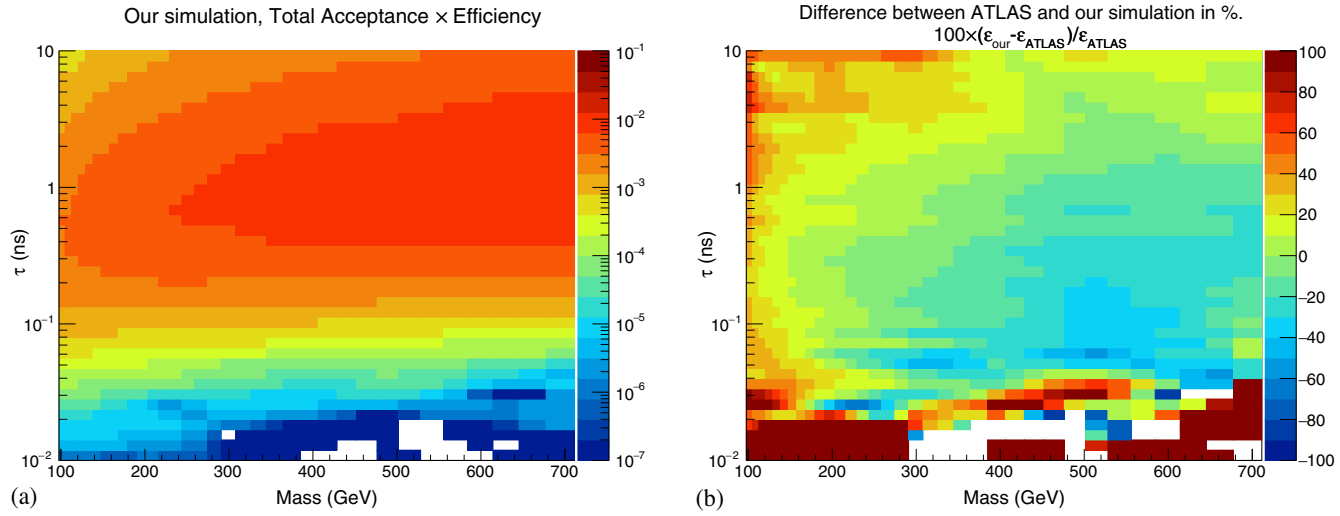

FIG. 4. (a) Total acceptance × efficiency in the electroweak channel ($E_A \times E_E \times T_A \times T_E$) from our simulation. b) Difference of the total acceptance × efficiency in % between our simulation and ATLAS: $(\epsilon_{\text{our}} - \epsilon_{\text{ATLAS}})/\epsilon_{\text{our}} \times 100$

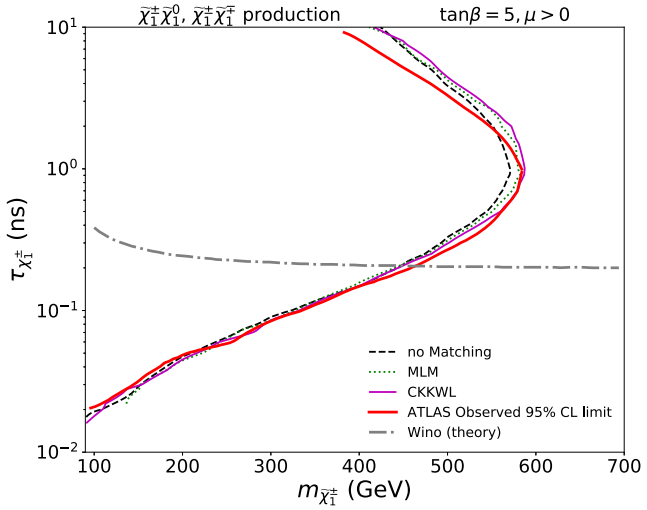

FIG. 5. Exclusion limits in the chargino life-time vs mass of chargino plane from ATLAS (red line) and from our simulations. The dashed black line is the limit for which no matching or merging are used, the dotted green line is the result for MLM matching, and the continuous purple line is the limit for CKKW-L merging. The grey dashed line shows the theory curve of the chargino lifetime in the almost pure wino LSP scenario at the two-loop level [98].

background done by the ATLAS Collaboration, which indicates a total observed (expected) number of background events of 9 (11.8) for $p_T > 100$ GeV.

Finally, we need to further apply $P = 0.57$ to every chargino in our events.[9] We note that the ATLAS Collaboration has not taken full advantage of the events featuring two disappearing tracks. In such a case, they have decided to keep only the hardest tracklet in the event, hence applying a probability of $p(1, 1)$ to it.

The final results of our validation are then shown in Fig. 5, where we compared the results from our simulation with the ATLAS exclusion limit, which is shown in solid red. The black dashed line shows the results when no extra radiation at tree-level accuracy through matching or merging is included, i.e., when all radiation is modeled by parton showering alone. We note that for lower lifetimes, all limits agree very well with each other. For larger τ (above 1 ns), the difference between ATLAS and our limit increases but still stays below 10% level (for the limit on a chargino mass for a given lifetime value). We can also see that generating samples with up to 1 extra parton in the matrix element is enough to reproduce ATLAS limits with quite a good accuracy.

Using the CKKW-L merging scheme yields the more accurate agreement with the ATLAS result. The MLM scheme performs slightly worse. In particular, for a nominal wino lifetime of 0.2 ns, we obtain an upper bound on the wino mass of 444 GeV, instead of the 458 GeV result from ATLAS, hence, a 3% difference in mass and 15% in the signal cross section where we are sensitive. We have also verified that the use of an appropriate matching procedure is necessary to obtain consistent exclusion limits, especially for wino masses above 450 GeV.

The ATLAS Collaboration has also interpreted the results of their study in the context of Higgsino dark matter [71]. Hence, their results provide an additional check for our procedure. They have only displayed their recasting in the 100–200 GeV range; this is why we will only compare the Higgsino model in this range. We show our results and those of the ATLAS Collaboration in Fig. 6.

We see that there is a good agreement between our reinterpretation and the ATLAS results in the whole mass range, where the largest differences do not exceed 10%. We see that for a fixed $c\tau$, ATLAS excludes a larger mass; hence, our recasting turns up to be on the conservative side. We have also checked that 40% difference in efficiencies between ATLAS and our simulations lead to less than 5% difference in the limits on the mass of the charged DM partner. We would like to note that the limits we have established in this study depend on the QCD scale that we fixed to be an invariant mass of $DD^\pm$ or $D^\mp D^\pm$ pair (depending on the production process). We have found that the choice of different QCD scale, for example, $Q = M_{\rm DM}$, leads to about 30% weaker limit because of the lower efficiency. This uncertainty should be kept in mind when using the limits on the cross section we provide in Appendix C.

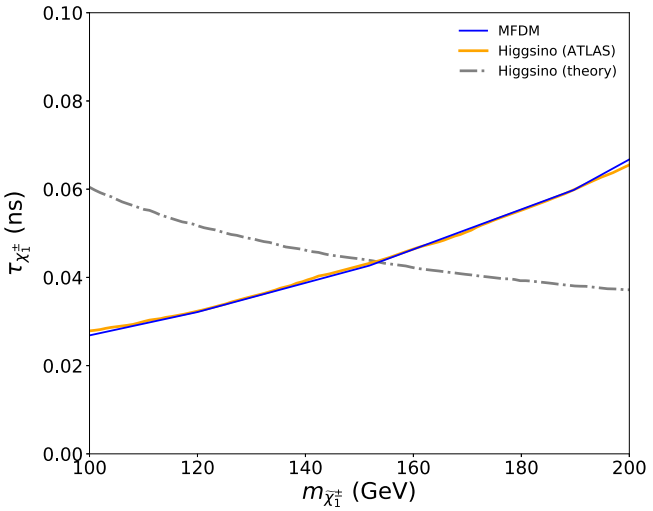

FIG. 6. Comparison between the official ATLAS reinterpretation of the disappearing track study in the Higgsino scenario (solid orange) and our recasting procedure. The solid blue shows our results, using NLO cross sections from PROSPINO.

[9]We note that this value has only been presented for the three benchmark points. We assume it to be flat throughout the whole parameter space.

We close this section by concluding that our recasting procedure reproduces well the published ATLAS results for the wino and Higgsino models. The PYTHON code implementing this procedure, together with the corresponding instructions, is publicly available in [29]. In the next section, we will then apply this procedure to other models of dark matter.

IV. REINTERPRETATION FOR MINIMAL MODELS

In this section, we apply our validated recasting to a few selected examples of minimal models. We note that in many cases, this provides the best probe of the parameter space and the first *direct* constraints on long-lived electrically charged particles.

In all our models, we have two kind of constraints, those that arise from *direct* searches and from *indirect* effects. The current direct collider constraints tend to be mild and come mostly from LEP searches [99–102]. At the LHC, the production of dark sector particles would lead invariably to $E_T^{\rm miss}$ signals. We are focusing on cases where ΔM is small, and hence, $D^{\pm}$ is long-lived. Thus, any study in the $X + E_T^{\rm miss}$ class (where X is some combination of SM particles) does not apply, *if X arises from intra dark-sector decays*, since X will be too soft to be detected. Nonetheless, X can arise through initial state radiation. The highest rates for $X + E_T^{\rm miss}$ signature is for the monojet final state (which is to a good approximation independent of the small mass splittings in the dark sector and does not depend on $c\tau$), which provides a robust lower limit on the dark sector mass scale for a given model.[10]

The indirect constraints that apply arise from either electroweak precision data (e.g: Peskin-Takeuchi S, T, U parameters) or from 1-loop effects from our charged particles in $b \to s\gamma$ decays. We note that these constraints are weak, as they can be reduced by additional contributions not explicitly involved the dark matter dynamics. For instance, in supersymmetric models, this rare decay proceeds via a chargino-stop loop, and the stop sector does not play any role in the dark matter phenomenology. Due to their strong model-dependence, we will ignore these constraints in what follows.

We display in Fig. (7a), the production cross section of pairs of particles: (dotted line) charged-charged, (dashed line) neutral-charged, and (continuous line) the sum of both contributions, for the vector (VTDM), fermion (MFDM), and scalar (i2HDM) model. In Fig. (7b), we show the analogous plot, for the wino and MFDM models.

Furthermore, in the Fig. (7c), we show, for the DD + jet process with $p_T(j) > 100$ GeV, the p_T distribution of the charged dark particle at parton level normalized to the cross section, while in the Fig. (7d), we present this distribution convoluted with the experimental efficiency for the reconstruction of the charged track (note that the latter does depend on the lifetime of D, while the former does not). From the figure, we see that the spectrum is much harder for vectors than for scalars and fermions. Given that the vector model also enjoys the largest cross section, we can expect the most stringent exclusions to occur for the VTDM. The p_T spectrum in the fermionic models is softer than in the i2HDM model. However, the cross section for fermion DM production are larger than that for scalar DM by about an order of magnitude. Hence, we can naively expect that fermionic models will follow after VTDM in the hierarchy of constraints. Scalar models will presumably have the mildest constraints.

In Fig. 8, we present the current LHC potential to probe the $(\tau_{D^{\pm}} - M_{D^{\pm}})$ parameter space of the MFDM, VTDM, wino, and i2HDM models with the disappearing track signature. We further superimpose the limits from the current [105] and future monojet searches as obtained using [106] results.[11] The colored lines show the bound obtained from our reinterpretation of the disappearing track search for each model. The solid ticks indicate the corresponding limit from the LHC monojet searches for the specified luminosity.[12]

We see that constraints derived from our reinterpretation of the disappearing track search probe a vast region of the parameter space, well beyond other LHC or LEP searches. We stress again that for 36 fb^{-1} LHC data, we have found the limit $m_\chi > 447$ GeV and $m_\chi > 152$ GeV at 95% C.L. for a fermionic triplet (MSSM wino) and doublet (MSSM Higgsino) model, respectively, which is in good agreement with the official results from ATLAS (460 GeV and 150 GeV, respectively). Note that these current limits are even stronger that the projected HL-LHC mass reach for

[10]For $c\tau \gtrsim 1m$, there are important constraints coming from heavy stable charged particle searches (HSCP) [103,104]. We note, however, that the focus of this paper is on tracks with nominal lifetime between 0.01 and 1 ns, namely a proper displacement of 3 mm–30 cm. For a lifetime of 30 cm and electrically charged particles, the HSCP does not yield competitive constraints.

[11]We have verified for several benchnmark points that the results of [106] are in good agreement with CheckMATE2 [107].

[12]A comment on the reinterpretation of monojet searches for long-lived charged particles is in order, regarding how the $D^{\pm}$ particles pass the event selection, depending on their lifetime. Since missing energy is computed in [105] from visible calorimeter deposits, for very low lifetimes, where $D^{\pm}$ gives only very little (or zero) pixel hits ($c\tau \lesssim 1$ mm), the prompt analysis can be directly applied. As the lifetime increases, however, the $D^{\pm}$ appears with more and more tracker hits, and even with calorimeter deposits due to the exponential decay tail. In that case, it is clear that the $D^{\pm}$ will not satisfy the loose jet selection criteria [108] adopted in the monojet study, where such events are discarded. Hence, we expect that the monojet limit will degrade for larger lifetimes; however, its proper assessment is outside the scope of this work.

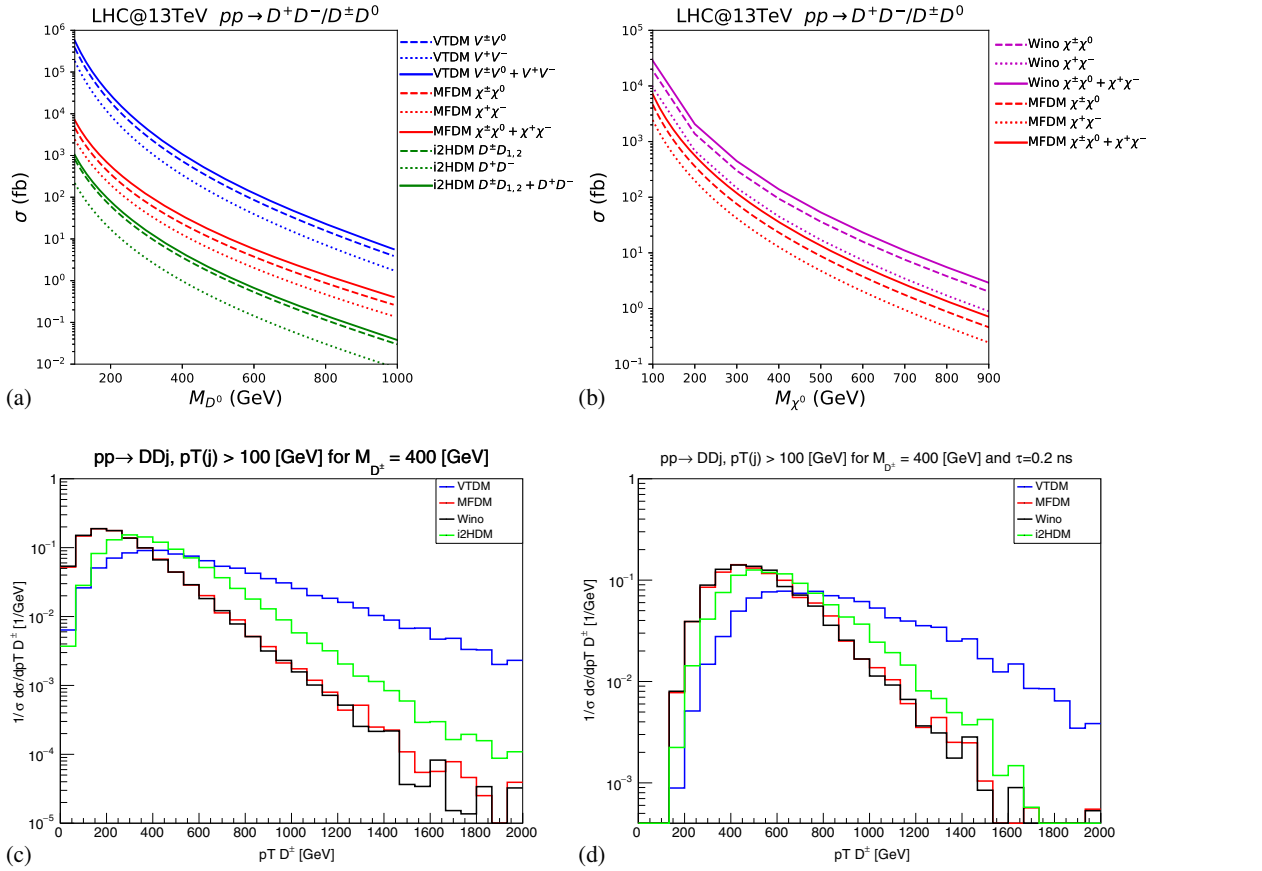

FIG. 7. (a) and (b) Production cross section for the charged-neutral ($D^\pm D$) and charged-charged (D^+D^-) pair production of dark sector particles in the models under consideration, as a function of the charged dark particle mass. (c) Transverse momentum distribution of the short-lived charged dark particle ("chargino") at the parton level. (d) Transverse momentum distribution of the reconstructed charged track.

monojet searches. In the VTDM model, disappearing tracks set a lower bound on 530 GeV for the nominal lifetime of 0.06 ns ($c\tau \sim 2$ cm)[13] For the i2HDM model, the strongest limit is 237 GeV, which corresponds to a lifetime of 0.53 ns and $\Delta M = 0.157$ MeV. This limit is larger than the estimated HL-LHC reach of about 190 GeV using a monojet [106].

We summarize these results in Table II, where we present the maximum excluded mass for each model under our scrutiny. We see that our intuition regarding the constraint hierarchy for the different models is confirmed.

The high potential of this LHC LLP study shows the paramount importance of not only conducting this class of searches but also of clarifying the analysis assumptions (object definitions, model cross sections used) and the required ingredients (efficiencies) for its prompt reinterpretation in the context of arbitrary models.

[13]The limit on DM mass from VTDM found in [43] was recently corrected (there was a typo in the analysis code) and agrees well with the more accurate estimation we found in this paper.

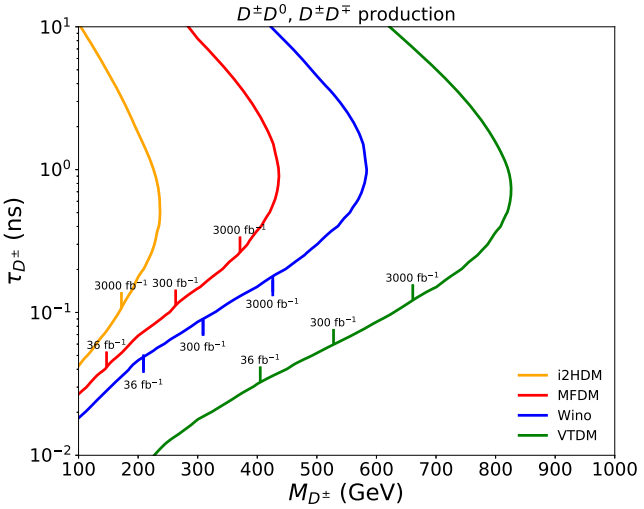

FIG. 8. Constraints on the parameter space of the dark sector models studies in this paper. The colored lines show the 95% exclusion reach of the LHC obtained from the reinterpretation of the disappearing track ATLAS study (36 fb^{-1}) for different models. The solid ticks indicate the constraints from LHC monojet searches at 36 fb^{-1} and projections for these searches for 300 and 3000 fb^{-1}.

TABLE II. Maximum excluded mass for different DM models, from our reinterpretation of the ATLAS disappearing track search with 36.1 fb^{-1} of data.

Models	Mass (GeV)	Tau (ns)
i2HDM	237	0.5
MFDM	436	0.9
VTDM	822	0.7
WINO	587	1.0

V. CONCLUSIONS

In this work, we have performed detailed studies devoted to the reinterpretation of the current disappearing track searches at the LHC for a wide class of models, going beyond the vanilla examples of Higgsino and wino dark matter.

We have validated our reinterpretation procedure by carefully following the ATLAS study [13] and reproduced, to good accuracy, their published results for wino dark matter. By using the provided efficiency heatmaps in the mass-lifetime chargino plane, we were able to obtain a good agreement with the ATLAS results, being a few percent away in most of the parameter space, with the largest differences taking place for lifetimes of about 1 ns. We have further studied the impact of smearing the parton level charged track momenta, which we have found to be a subpercent effect. An accurate description of multijet final states is necessary for a precise description of the data. We conclude that tree-level calculation for at least one additional hard jet is necessary to define the signal and that the CKKW-L merging scheme (which may be considered more predictive if additional QCD radiation can be very hard) allows us to perform more accurate simulation of the two-tracklet system. The modeling of the transition region of moderate jet separation can be important, in particular before the tracklet selection, which led us to assess the matching-dependence of the results by using two different merging schemes. Finally, we have also validated our procedure for the Higgsino study, following the ATLAS reinterpretation of their own results [71].

With our validated procedure, we have reinterpreted the disappearing track search in the context of several models of dark matter: the minimal fermion doublet model (MFDM), the vector dark matter model (VTDM), and the inert 2-Higgs doublet model (i2HDM). Our results shown in Fig. 8 are the core result of this paper. As by-products of our analysis, we also provide (a) our upper limits and efficiencies on the lifetime-mass plane of the different dark matter models considered here and (b) the PYTHON code used for our analysis, in [29], which is ready to run over event samples of arbitrary DM models.

It is worth stressing that while most of the information about the ATLAS study was publicly available, close contact with the experimentalists that carried out the study was still required, in order to understand a few crucial details. Our interaction with our experimental colleagues has been very fruitful and helped considerably in explaining the study and in dispelling doubts. However, it would desirable that a reinterpretation of an experimental study does not require us to consult with the experts from the experimental collaborations. Going into details, the multiple definitions of efficiencies and acceptances were not immediately clear to us. As these are terms that are burdened by various interpretations, we encourage the experimental collaborations to define these quantities with mathematical formulas that are universally understood and not prone to a language interpretation. These considerations also apply to the definition of observables at the different simulation and reconstruction levels. Furthermore, a key ingredient for the comparison with the benchmark model(s) chosen by the Collaboration is to also report the assumed cross section values, as often it is not clear the exact parameters used as input to the state-of-the-art radiative corrections software package: not only model parameters, but also, for instance, which PDF set was used or which central merging scale values were considered.

One should also note that the disappearing track analysis (as any long-lived study) can resolve the different lifetimes, while a positive signal in a prompt study does only inform on the mass scale on a given model but provides no information on the specific lifetime.

We stress that the disappearing track signature provides a unique opportunity for the most sensitive test of DM parameter space if long-lived DM charged partners of DM occurs in the model. This sensitivity outshines the LHC monojet constraints, which even for their HL-LHC have a weaker sensitivity to the parameter space. Being concrete, in this study, we have found lower bounds on the charged particle mass of 530 GeV for the nominal lifetime of 0.07 ns ($c\tau \sim 2$ cm) in the VTDM model, going well beyond the 100 GeV limit set by LEP. In the i2HDM model, we have found that for $\tau > 0.4$ ns the 95% C.L sets a scale of about 237 GeV for a lifetime of 0.5 ns, while for $\tau = 0.05$ ns the limit degrades to 115 GeV.

ACKNOWLEDGMENTS

Recently, CMS has made public a new disappearing track study [109], and the public reinterpretation material was only made public in July [110]. Given the important differences between ATLAS and CMS in a) their inner tracker configurations and b) the analysis strategy, we leave the recasting of the CMS results for future work. The authors acknowledge the use of the IRIDIS High Performance Computing Facility, and associated support services at the University of Southampton, in the completion of this work. We are indebted to Ryu Sawada for his valuable help with understanding the details of the ATLAS analysis. We also would like to thank Giovanna Cottin and Nishita Desai for useful discussions, and Andre Lessa for

TABLE III. Reconstruction event cuts. The transverse energy is defined as $E_T = \sqrt{m^2 + P_T^2}$. When no cut is applied, we indicate it with "Cross mark"

	Transverse momentum (GeV)	Pseudorapidity	Transverse energy (GeV)
Jet	$P_T > 20$	$\|\eta\| < 2.8$	✗
Muons	$P_T > 10$	$\|\eta\| < 2.7$	✗
Electrons	✗	$\|\eta\| < 2.47$	$E_T > 10$
Charginos	$P_T > 5$	$\|\eta\| < 2.5$	✗

help with uploading our code to the LLP Recasting Repository, for the useful suggestions to improve the code and for being our first beta tester. A. B. acknowledges partial support from the STFC Grant No. ST/L000296/1 and the Soton-FAPESP grant. AB also thanks the NExT Institute and Royal Society International Exchange Grant No. IEC-R2-202018. F. R. acknowledges Funding for Postdoctoral research in Southampton University, United Kingdom, CONICYT Grant No. 74180065. This work has been supported by the Mainz Institute for Theoretical Physics (MITP) of the Cluster of Excellence PRISMA+ (Project No. 39083149). S. P. gratefully acknowledges funding from the Swedish Research Council, under Contract No. 2016-05996.

APPENDIX A: OBJECT RECONSTRUCTION

In order to ensure the reproducibility of our results, we explicitly list here the kinematical cuts applied on jets, electrons, and muons following [13]. The selection for neutralinos, neutrinos, and charginos was performed separately taking the data from the branch *particle* in the Delphes output, which takes the information directly from PYTHIA8. Since these objects are crucial for the study, we deemed appropriate to explain their treatment in the main text.

1. Jets, electrons, muons, and charginos

In Table III, we show the implemented cuts on the transverse momenta P_T, pseudorapidity η and transverse energy E_T applied to jets, muons, electrons, and charginos in the reconstruction stage. In addition to the cuts listed in the table above, we also applied the following criteria when dealing with overlaps between the different objects:

(i) If ΔR between a jet and an electron candidate is less than 0.2, the jet is discarded.
(ii) If an electron and a jet candidate are found between $0.2 < \Delta R < 0.4$, the electron is discarded.
(iii) If a muon and a jet candidate are found between $0.2 < \Delta R < 0.4$, the muon is discarded.
(iv) If ΔR between a jet and a muon candidate is less than 0.2, the jet is discarded.

APPENDIX B: MATCHING PROCEDURE

In Fig. 9, we present the distribution of the transverse momentum of the leading jet and a pair of neutralinos using two matching schemes: CKKW-L (blue) and MLM (red), using a chargino mass of $M_{\chi^\pm} = 400$ GeV and a merging scale of $t_{\rm ms} = 100$ GeV. Samples with a zero and one additional jet at the matrix element level are employed.

At both small and large transverse momenta, the distributions converge, as expected by the requirement that

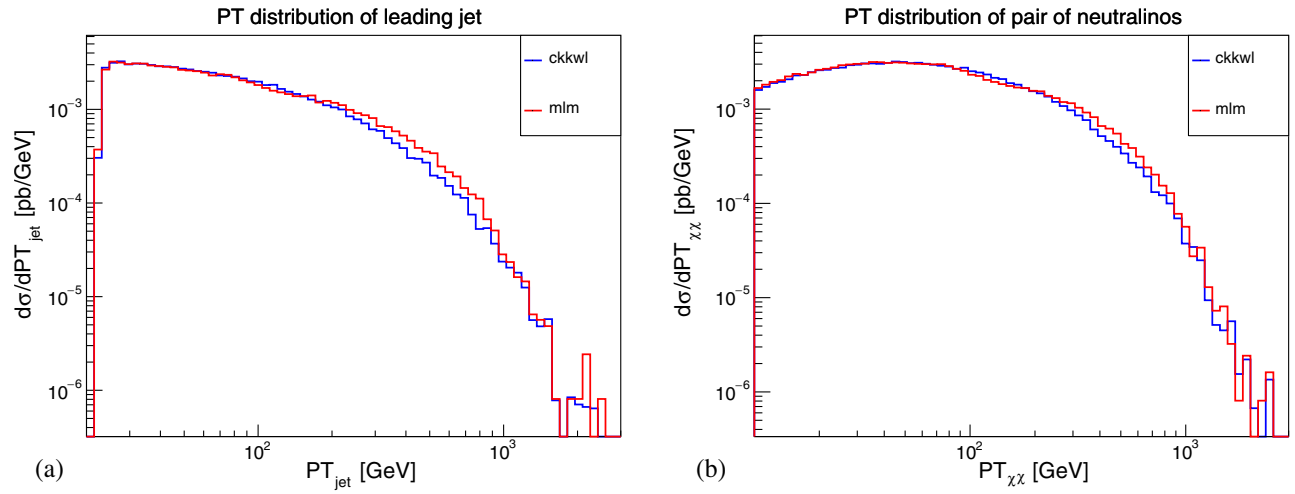

FIG. 9. Transverse momenta distribution p_T of (a) the leading jet and (b) pair of neutralinos using CKKW-L (blue) and MLM (red) matching schemes. In this example, $M_{\chi^\pm} = 400$ GeV, and the merging scale parameter was set to 100 GeV.

TABLE IV. Event and tracklet acceptances and efficiencies for the three benchmarks points used by ATLAS, when employing CKKW-L merging or MLM matching.

ATLAS benchmark points								
Signal	Event				Tracklet			
	E_A		E_E		T_A		T_E	
$m_\chi^\pm$ (GeV)	ckkwl	mlm	ckkwl	mlm	ckkwl	mlm	ckkwl	mlm
400	0.0879	0.0815	1.030	1.021	0.08	0.08	0.44	0.44
600	0.1025	0.0996	1.054	1.035	0.06	0.06	0.44	0.44
600	0.1025	0.0996	1.054	1.035	0.22	0.22	0.44	0.44

tree-level results for the inclusive production and production in association with one jet should be recovered. However, in the rather extended transition region, visible differences appear. The fist important difference we can observe in both plots is that the MLM scheme present a small valley just after the merging scale at 100 GeV, showing the mismatch between the zero- and one-jet sample. This effect is related to details of the jet matching method. The overlap removal strategy by MLM jet matching induces a non-negligible matching scale dependence, which is not analytically tractable, and thus difficult to predict. "Tuning" of the matching scale, e.g., based on previous experience and reference predictions, can help ameliorate this problem. Similar comments apply for mismatches of renormalization and factorization scales used at fixed order and in the parton shower.

These mismatches are, in principle, absent in the CKKW-L scheme. Indeed, we observe a much smoother transition at the merging scale, for all merging scale values. This leads us to favor CKKW-L for predictions. However, a comparison to MLM results can be very informative, by allowing us to identify the transition region. The absence of mismatches in scale setting in CKKW-L is due to the fact that the parton-shower scale setting procedure is employed throughout phase space; i.e., fixed-order results are reweighted to implement the scale setting. Since the parton-shower scale setting is based on interpreting phase-space points as sequence of single emissions, the resulting scales can lead to unrealistic results for phase-space points that do not follow a simple parton-shower interpretation. In this case, more intricate mechanisms have to be considered [90]. For the present study, the impact of such "unordered states" is not crucial, as, e.g., shown by comparison with results of the MLM scheme.

Given the complex selection criteria for the event and tracklet selections, it is not obvious how relevant the differences between matching schemes are in practise. Table IV lists acceptances and efficiencies for two matching schemes. Overall, matching scheme differences have larger impact for low $m_\chi^\pm$ masses, and for "more inclusive" *event* selection criteria, reaching up to 7.3% for E_A. The acceptance under these criteria include contributions from regions of moderate as well as large jet separation. The dependence on the moderate-separation transition region is removed by the more aggressive tracklet selection. This selection effectively only relies on an accurate model of configurations with two well-separated jets. There is little matching scheme variation in this region, as can be seen in the right-hand edges of both jet spectra in Fig. 9.

APPENDIX C: UPPER LIMITS AND EFFICIENCIES

In this section, we show tables with efficiencies and excluded regions presented as upper limits on the two body production cross section (in fb) in the lifetime (in nanoseconds)—dark matter mass (in GeV) plane for the four

TABLE V. Efficiency table for the i2HDM model.

Tau (ns)	Mass (GeV)						
	100	200	300	400	500	600	700
0.01	1.37×10^{-6}	1.90×10^{-7}	5.64×10^{-8}	1.86×10^{-8}	1.17×10^{-8}	2.59×10^{-11}	2.41×10^{-9}
0.02	2.31×10^{-5}	9.19×10^{-6}	4.13×10^{-6}	2.26×10^{-6}	1.46×10^{-6}	6.29×10^{-7}	3.84×10^{-7}
0.03	8.67×10^{-5}	5.20×10^{-5}	3.10×10^{-5}	2.06×10^{-5}	1.43×10^{-5}	8.99×10^{-6}	6.72×10^{-6}
0.04	1.90×10^{-4}	1.43×10^{-4}	1.02×10^{-4}	7.52×10^{-5}	5.61×10^{-5}	4.06×10^{-5}	3.24×10^{-5}
0.05	3.19×10^{-4}	2.83×10^{-4}	2.27×10^{-4}	1.77×10^{-4}	1.42×10^{-4}	1.10×10^{-4}	9.33×10^{-5}
0.06	4.63×10^{-4}	4.60×10^{-4}	4.00×10^{-4}	3.34×10^{-4}	2.78×10^{-4}	2.25×10^{-4}	1.98×10^{-4}
0.07	6.14×10^{-4}	6.67×10^{-4}	6.15×10^{-4}	5.32×10^{-4}	4.61×10^{-4}	3.89×10^{-4}	3.47×10^{-4}

(Table continued)

TABLE V. *(Continued)*

Tau (ns)	Mass (GeV)						
	100	200	300	400	500	600	700
0.08	7.61×10^{-4}	8.84×10^{-4}	8.60×10^{-4}	7.71×10^{-4}	6.84×10^{-4}	5.94×10^{-4}	5.45×10^{-4}
0.09	9.01×10^{-4}	1.11×10^{-3}	1.12×10^{-3}	1.04×10^{-3}	9.44×10^{-4}	8.40×10^{-4}	7.79×10^{-4}
0.10	1.03×10^{-3}	1.35×10^{-3}	1.40×10^{-3}	1.32×10^{-3}	1.23×10^{-3}	1.12×10^{-3}	1.05×10^{-3}
0.20	1.83×10^{-3}	3.18×10^{-3}	3.92×10^{-3}	4.23×10^{-3}	4.37×10^{-3}	4.37×10^{-3}	4.40×10^{-3}
0.30	2.05×10^{-3}	4.07×10^{-3}	5.39×10^{-3}	6.12×10^{-3}	6.63×10^{-3}	6.91×10^{-3}	7.12×10^{-3}
0.40	2.05×10^{-3}	4.41×10^{-3}	6.08×10^{-3}	7.13×10^{-3}	7.92×10^{-3}	8.45×10^{-3}	8.85×10^{-3}
0.50	1.96×10^{-3}	4.47×10^{-3}	6.36×10^{-3}	7.60×10^{-3}	8.61×10^{-3}	9.31×10^{-3}	9.85×10^{-3}
0.60	1.86×10^{-3}	4.41×10^{-3}	6.41×10^{-3}	7.77×10^{-3}	8.90×10^{-3}	9.73×10^{-3}	1.04×10^{-2}
0.70	1.75×10^{-3}	4.29×10^{-3}	6.33×10^{-3}	7.75×10^{-3}	8.97×10^{-3}	9.89×10^{-3}	1.06×10^{-2}
0.80	1.64×10^{-3}	4.14×10^{-3}	6.19×10^{-3}	7.64×10^{-3}	8.91×10^{-3}	9.88×10^{-3}	1.06×10^{-2}
0.90	1.55×10^{-3}	3.98×10^{-3}	6.01×10^{-3}	7.47×10^{-3}	8.76×10^{-3}	9.78×10^{-3}	1.05×10^{-2}
1.00	1.46×10^{-3}	3.81×10^{-3}	5.82×10^{-3}	7.28×10^{-3}	8.59×10^{-3}	9.60×10^{-3}	1.04×10^{-2}
2.00	9.14×10^{-4}	2.60×10^{-3}	4.14×10^{-3}	5.34×10^{-3}	6.44×10^{-3}	7.39×10^{-3}	8.09×10^{-3}
3.00	6.61×10^{-4}	1.93×10^{-3}	3.14×10^{-3}	4.10×10^{-3}	5.00×10^{-3}	5.76×10^{-3}	6.35×10^{-3}
4.00	5.18×10^{-4}	1.54×10^{-3}	2.52×10^{-3}	3.31×10^{-3}	4.06×10^{-3}	4.70×10^{-3}	5.20×10^{-3}
5.00	4.26×10^{-4}	1.28×10^{-3}	2.10×10^{-3}	2.77×10^{-3}	3.41×10^{-3}	3.97×10^{-3}	4.38×10^{-3}
6.00	3.62×10^{-4}	1.09×10^{-3}	1.80×10^{-3}	2.39×10^{-3}	2.94×10^{-3}	3.43×10^{-3}	3.79×10^{-3}
7.00	3.16×10^{-4}	9.52×10^{-4}	1.58×10^{-3}	2.09×10^{-3}	2.58×10^{-3}	3.02×10^{-3}	3.33×10^{-3}
8.00	2.76×10^{-4}	8.44×10^{-4}	1.40×10^{-3}	1.86×10^{-3}	2.30×10^{-3}	2.69×10^{-3}	2.97×10^{-3}
9.00	2.49×10^{-4}	7.61×10^{-4}	1.27×10^{-3}	1.68×10^{-3}	2.08×10^{-3}	2.43×10^{-3}	2.69×10^{-3}
10.00	2.25×10^{-4}	6.88×10^{-4}	1.15×10^{-3}	1.52×10^{-3}	1.89×10^{-3}	2.21×10^{-3}	2.45×10^{-3}

TABLE VI. Efficiency table for the MFDM model.

Tau (ns)	Mass (GeV)							
	91	200	300	400	500	600	700	800
0.01	4.02×10^{-7}	8.58×10^{-8}	8.04×10^{-9}	9.59×10^{-9}	3.50×10^{-9}	0.00	0.00	0.00
0.02	9.40×10^{-6}	3.35×10^{-6}	1.27×10^{-6}	6.60×10^{-7}	3.26×10^{-7}	1.11×10^{-7}	6.49×10^{-8}	5.91×10^{-8}
0.03	3.78×10^{-5}	1.96×10^{-5}	9.88×10^{-6}	5.90×10^{-6}	4.05×10^{-6}	1.85×10^{-6}	1.32×10^{-6}	9.57×10^{-7}
0.04	8.89×10^{-5}	5.77×10^{-5}	3.60×10^{-5}	2.40×10^{-5}	1.74×10^{-5}	9.92×10^{-6}	7.70×10^{-6}	5.85×10^{-6}
0.05	1.57×10^{-4}	1.22×10^{-4}	8.37×10^{-5}	6.08×10^{-5}	4.71×10^{-5}	3.08×10^{-5}	2.51×10^{-5}	1.96×10^{-5}
0.06	2.35×10^{-4}	2.09×10^{-4}	1.57×10^{-4}	1.22×10^{-4}	9.82×10^{-5}	6.94×10^{-5}	5.71×10^{-5}	4.69×10^{-5}
0.07	3.20×10^{-4}	3.15×10^{-4}	2.54×10^{-4}	2.07×10^{-4}	1.72×10^{-4}	1.30×10^{-4}	1.10×10^{-4}	9.14×10^{-5}
0.08	4.08×10^{-4}	4.37×10^{-4}	3.74×10^{-4}	3.17×10^{-4}	2.69×10^{-4}	2.14×10^{-4}	1.87×10^{-4}	1.56×10^{-4}
0.09	4.94×10^{-4}	5.73×10^{-4}	5.06×10^{-4}	4.45×10^{-4}	3.87×10^{-4}	3.19×10^{-4}	2.83×10^{-4}	2.41×10^{-4}
0.10	5.78×10^{-4}	7.11×10^{-4}	6.55×10^{-4}	5.90×10^{-4}	5.23×10^{-4}	4.47×10^{-4}	4.04×10^{-4}	3.46×10^{-4}
0.20	1.13×10^{-3}	2.08×10^{-3}	2.34×10^{-3}	2.46×10^{-3}	2.40×10^{-3}	2.38×10^{-3}	2.31×10^{-3}	2.15×10^{-3}
0.30	1.32×10^{-3}	2.95×10^{-3}	3.65×10^{-3}	4.09×10^{-3}	4.19×10^{-3}	4.41×10^{-3}	4.40×10^{-3}	4.25×10^{-3}
0.40	1.35×10^{-3}	3.42×10^{-3}	4.47×10^{-3}	5.23×10^{-3}	5.50×10^{-3}	5.97×10^{-3}	6.07×10^{-3}	6.01×10^{-3}
0.50	1.32×10^{-3}	3.63×10^{-3}	4.94×10^{-3}	5.94×10^{-3}	6.38×10^{-3}	7.07×10^{-3}	7.29×10^{-3}	7.33×10^{-3}
0.60	1.26×10^{-3}	3.70×10^{-3}	5.20×10^{-3}	6.39×10^{-3}	6.96×10^{-3}	7.82×10^{-3}	8.13×10^{-3}	8.27×10^{-3}
0.70	1.20×10^{-3}	3.70×10^{-3}	5.31×10^{-3}	6.63×10^{-3}	7.30×10^{-3}	8.32×10^{-3}	8.70×10^{-3}	8.94×10^{-3}
0.80	1.14×10^{-3}	3.64×10^{-3}	5.32×10^{-3}	6.74×10^{-3}	7.51×10^{-3}	8.62×10^{-3}	9.08×10^{-3}	9.39×10^{-3}
0.90	1.08×10^{-3}	3.57×10^{-3}	5.29×10^{-3}	6.77×10^{-3}	7.60×10^{-3}	8.79×10^{-3}	9.31×10^{-3}	9.68×10^{-3}
1.00	1.02×10^{-3}	3.47×10^{-3}	5.22×10^{-3}	6.74×10^{-3}	7.62×10^{-3}	8.86×10^{-3}	9.44×10^{-3}	9.85×10^{-3}
2.00	6.64×10^{-4}	2.55×10^{-3}	4.08×10^{-3}	5.57×10^{-3}	6.54×10^{-3}	7.85×10^{-3}	8.57×10^{-3}	9.16×10^{-3}
3.00	4.87×10^{-4}	1.96×10^{-3}	3.22×10^{-3}	4.48×10^{-3}	5.37×10^{-3}	6.53×10^{-3}	7.21×10^{-3}	7.78×10^{-3}
4.00	3.85×10^{-4}	1.59×10^{-3}	2.64×10^{-3}	3.73×10^{-3}	4.50×10^{-3}	5.52×10^{-3}	6.13×10^{-3}	6.65×10^{-3}

(Table continued)

TABLE VI. *(Continued)*

Tau (ns)	Mass (GeV)							
	91	200	300	400	500	600	700	800
5.00	3.18×10^{-4}	1.33×10^{-3}	2.23×10^{-3}	3.17×10^{-3}	3.86×10^{-3}	4.76×10^{-3}	5.30×10^{-3}	5.78×10^{-3}
6.00	2.71×10^{-4}	1.15×10^{-3}	1.94×10^{-3}	2.76×10^{-3}	3.38×10^{-3}	4.17×10^{-3}	4.67×10^{-3}	5.10×10^{-3}
7.00	2.38×10^{-4}	1.01×10^{-3}	1.70×10^{-3}	2.45×10^{-3}	3.00×10^{-3}	3.72×10^{-3}	4.16×10^{-3}	4.55×10^{-3}
8.00	2.09×10^{-4}	8.99×10^{-4}	1.52×10^{-3}	2.19×10^{-3}	2.70×10^{-3}	3.35×10^{-3}	3.76×10^{-3}	4.11×10^{-3}
9.00	1.86×10^{-4}	8.11×10^{-4}	1.37×10^{-3}	1.98×10^{-3}	2.45×10^{-3}	3.04×10^{-3}	3.42×10^{-3}	3.75×10^{-3}
10.00	1.70×10^{-4}	7.39×10^{-4}	1.26×10^{-3}	1.82×10^{-3}	2.25×10^{-3}	2.79×10^{-3}	3.14×10^{-3}	3.45×10^{-3}

different DM Models studied previously. In particular, in Tables V, VI, and VII we present the efficiencies for i2HDM, MFDM and VTDM models respectively, while in Tables VIII, IX, and X we present the upper limits on the production cross sections respectively for these models. The cross section limits considered the unweighted sum of the channels: $pp \to D^+D^-$ and $pp \to D^\pm D^0$ and next-to-leading-order QCD corrections (k factor) only for the fermion model. One should note that for small lifetimes, the efficiencies for the various models can differ by an order of magnitude. This is due to the fact that for small lifetimes large boosts are required, which strongly depend on the p_T distributions of the $D^\pm$ particles. As shown in Fig. 7(d), these distributions differ considerably among the different models studied here. One note that the limits depend on the QCD scale, which we fixed to be an invariant mass of $DD^\pm$ or $D^\mp D^\pm$ pair. The choice of different QCD scale, for example, $Q = M_{\rm DM}$, leads to about 30% weaker limit because of the lower efficiency. Please keep this uncertainty in mind when using the limits we provide here.

TABLE VII. Efficiency table for the VTDM model.

Tau (ns)	Mass (GeV)							
	100	200	300	400	500	600	700	800
0.01	2.27×10^{-4}	2.12×10^{-5}	3.45×10^{-6}	6.90×10^{-7}	1.53×10^{-7}	5.27×10^{-8}	1.06×10^{-8}	1.10×10^{-10}
0.02	1.17×10^{-3}	2.92×10^{-4}	8.53×10^{-5}	3.42×10^{-5}	1.42×10^{-5}	7.05×10^{-6}	3.39×10^{-6}	1.73×10^{-6}
0.03	2.22×10^{-3}	8.57×10^{-4}	3.39×10^{-4}	1.77×10^{-4}	9.47×10^{-5}	5.58×10^{-5}	3.10×10^{-5}	1.94×10^{-5}
0.04	3.10×10^{-3}	1.54×10^{-3}	7.49×10^{-4}	4.56×10^{-4}	2.86×10^{-4}	1.87×10^{-4}	1.15×10^{-4}	7.82×10^{-5}
0.05	3.78×10^{-3}	2.26×10^{-3}	1.27×10^{-3}	8.49×10^{-4}	5.83×10^{-4}	4.09×10^{-4}	2.76×10^{-4}	1.99×10^{-4}
0.06	4.31×10^{-3}	2.93×10^{-3}	1.82×10^{-3}	1.31×10^{-3}	9.68×10^{-4}	7.19×10^{-4}	5.14×10^{-4}	3.87×10^{-4}
0.07	4.71×10^{-3}	3.55×10^{-3}	2.40×10^{-3}	1.83×10^{-3}	1.41×10^{-3}	1.10×10^{-3}	8.23×10^{-4}	6.36×10^{-4}
0.08	5.02×10^{-3}	4.09×10^{-3}	2.95×10^{-3}	2.35×10^{-3}	1.90×10^{-3}	1.52×10^{-3}	1.19×10^{-3}	9.40×10^{-4}
0.09	5.23×10^{-3}	4.57×10^{-3}	3.48×10^{-3}	2.88×10^{-3}	2.40×10^{-3}	1.99×10^{-3}	1.60×10^{-3}	1.29×10^{-3}
0.10	5.39×10^{-3}	5.00×10^{-3}	3.98×10^{-3}	3.39×10^{-3}	2.91×10^{-3}	2.47×10^{-3}	2.03×10^{-3}	1.67×10^{-3}
0.20	5.54×10^{-3}	6.99×10^{-3}	7.08×10^{-3}	7.11×10^{-3}	7.04×10^{-3}	6.79×10^{-3}	6.35×10^{-3}	5.79×10^{-3}
0.30	4.98×10^{-3}	7.23×10^{-3}	8.09×10^{-3}	8.70×10^{-3}	9.13×10^{-3}	9.27×10^{-3}	9.15×10^{-3}	8.73×10^{-3}
0.40	4.41×10^{-3}	6.97×10^{-3}	8.26×10^{-3}	9.24×10^{-3}	1.00×10^{-2}	1.05×10^{-2}	1.07×10^{-2}	1.04×10^{-2}
0.50	3.94×10^{-3}	6.57×10^{-3}	8.08×10^{-3}	9.28×10^{-3}	1.03×10^{-2}	1.10×10^{-2}	1.14×10^{-2}	1.13×10^{-2}
0.60	3.55×10^{-3}	6.14×10^{-3}	7.78×10^{-3}	9.09×10^{-3}	1.02×10^{-2}	1.11×10^{-2}	1.16×10^{-2}	1.17×10^{-2}
0.70	3.23×10^{-3}	5.75×10^{-3}	7.43×10^{-3}	8.80×10^{-3}	1.00×10^{-2}	1.10×10^{-2}	1.16×10^{-2}	1.18×10^{-2}
0.80	2.95×10^{-3}	5.39×10^{-3}	7.08×10^{-3}	8.48×10^{-3}	9.73×10^{-3}	1.07×10^{-2}	1.15×10^{-2}	1.18×10^{-2}
0.90	2.72×10^{-3}	5.07×10^{-3}	6.74×10^{-3}	8.14×10^{-3}	9.42×10^{-3}	1.05×10^{-2}	1.13×10^{-2}	1.16×10^{-2}
1.00	2.52×10^{-3}	4.76×10^{-3}	6.41×10^{-3}	7.80×10^{-3}	9.10×10^{-3}	1.01×10^{-2}	1.10×10^{-2}	1.13×10^{-2}
2.00	1.45×10^{-3}	2.96×10^{-3}	4.21×10^{-3}	5.32×10^{-3}	6.41×10^{-3}	7.35×10^{-3}	8.18×10^{-3}	8.64×10^{-3}
3.00	1.02×10^{-3}	2.14×10^{-3}	3.11×10^{-3}	3.98×10^{-3}	4.86×10^{-3}	5.64×10^{-3}	6.34×10^{-3}	6.76×10^{-3}
4.00	7.91×10^{-4}	1.68×10^{-3}	2.47×10^{-3}	3.17×10^{-3}	3.90×10^{-3}	4.55×10^{-3}	5.15×10^{-3}	5.52×10^{-3}
5.00	6.42×10^{-4}	1.38×10^{-3}	2.03×10^{-3}	2.63×10^{-3}	3.26×10^{-3}	3.81×10^{-3}	4.33×10^{-3}	4.65×10^{-3}
6.00	5.42×10^{-4}	1.17×10^{-3}	1.73×10^{-3}	2.26×10^{-3}	2.80×10^{-3}	3.28×10^{-3}	3.73×10^{-3}	4.02×10^{-3}
7.00	4.68×10^{-4}	1.02×10^{-3}	1.51×10^{-3}	1.97×10^{-3}	2.45×10^{-3}	2.87×10^{-3}	3.28×10^{-3}	3.53×10^{-3}
8.00	4.12×10^{-4}	8.95×10^{-4}	1.34×10^{-3}	1.75×10^{-3}	2.18×10^{-3}	2.56×10^{-3}	2.93×10^{-3}	3.15×10^{-3}
9.00	3.69×10^{-4}	8.05×10^{-4}	1.20×10^{-3}	1.58×10^{-3}	1.95×10^{-3}	2.31×10^{-3}	2.63×10^{-3}	2.85×10^{-3}
10.00	3.32×10^{-4}	7.26×10^{-4}	1.09×10^{-3}	1.42×10^{-3}	1.78×10^{-3}	2.11×10^{-3}	2.40×10^{-3}	2.59×10^{-3}

TABLE VIII. Upper limits for production cross section in fb for the i2HDM model.

Tau (ns)	Mass (GeV)						
	100	200	300	400	500	600	700
0.01	1.61×10^5	1.16×10^6	3.90×10^6	1.19×10^7	1.88×10^7	8.49×10^9	9.12×10^7
0.02	9506	23930	53300	97200	1.51×10^5	3.50×10^5	5.73×10^5
0.03	2537	4230	7092	10690	15340	24460	32760
0.04	1156	1533	2161	2926	3924	5416	6791
0.05	689.4	778.7	968.7	1242	1554	2006	2359
0.06	475.3	478.6	549.9	659.2	792.6	975.7	1112
0.07	358.5	330.1	357.6	413.4	476.7	565.8	633.3
0.08	289.3	248.9	255.7	285.2	321.9	370.6	404.0
0.09	244.1	197.5	195.9	212.1	233.0	261.8	282.3
0.10	213.1	163.5	157.1	166.3	178.7	196.7	209.7
0.20	119.9	69.09	56.13	52.06	50.38	50.31	50.03
0.30	107.1	54.02	40.82	35.95	33.20	31.85	30.89
0.40	107.5	49.93	36.19	30.85	27.76	26.03	24.85
0.50	112.2	49.16	34.59	28.95	25.56	23.64	22.34
0.60	118.4	49.85	34.35	28.32	24.72	22.61	21.21
0.70	125.9	51.28	34.74	28.38	24.53	22.25	20.76
0.80	134.0	53.16	35.54	28.78	24.69	22.27	20.69
0.90	141.8	55.28	36.58	29.44	25.11	22.50	20.86
1.00	150.7	57.70	37.81	30.21	25.62	22.91	21.17
2.00	240.7	84.71	53.11	41.19	34.15	29.78	27.19
3.00	332.6	114.0	70.02	53.61	44.03	38.18	34.63
4.00	425.0	143.0	87.26	66.39	54.24	46.78	42.32
5.00	516.6	172.4	104.6	79.31	64.56	55.40	50.21
6.00	608.3	201.9	122.1	92.24	74.80	64.15	58.07
7.00	697.2	231.1	139.4	105.2	85.16	72.91	66.03
8.00	796.2	260.7	156.7	118.1	95.52	81.71	73.98
9.00	885.1	289.2	173.7	131.0	105.6	90.54	81.93
10.00	978.6	319.6	191.9	144.3	116.2	99.56	89.98

TABLE IX. Upper limits for production cross section in fb for the MFDM model. Cells with entry "Three center dots" contain an infinite upper limit (i.e. no sensitivity). This is due to a vanishing efficiency in the corresponding cell of the efficiency table, which in turn is a consequence of the low statistic of the heatmap used to describe the analysis.

Tau (ns)	Mass (GeV)							
	91	200	300	400	500	600	700	800
0.01	5.46×10^5	2.56×10^6	2.73×10^7	2.29×10^7	6.28×10^7	⋯	⋯	⋯
0.02	2.34×10^4	6.56×10^4	1.74×10^5	3.34×10^5	6.75×10^5	1.98×10^6	3.39×10^6	3.72×10^6
0.03	5815	1.12×10^4	22280	37310	54380	119200	166700	230000
0.04	2474	3812	6119	9178	12670	22170	28580	37600
0.05	1404	1805	2628	3621	4673	7152	8770	11220
0.06	937.9	1051	1404	1806	2240	3172	3852	4688
0.07	687.7	698.4	865	1064	1278	1689	1999	2406
0.08	539.6	503.4	588.8	694.8	818.3	1028	1179	1408
0.09	445.8	384.1	435.1	493.9	568.5	690.4	777.3	913.7
0.10	380.8	309.2	336.0	372.7	420.9	492.2	545.0	635.5
0.20	194.1	106.0	94.0	89.53	91.84	92.38	95.35	102.4
0.30	166.9	74.47	60.23	53.76	52.55	49.92	50.02	51.71
0.40	163.1	64.41	49.20	42.09	40.03	36.87	36.23	36.60
0.50	167.2	60.56	44.54	37.04	34.48	31.14	30.18	30.01
0.60	174.7	59.39	42.30	34.45	31.62	28.15	27.05	26.59

(Table continued)

TABLE IX. *(Continued)*

Tau (ns)	Mass (GeV)							
	91	200	300	400	500	600	700	800
0.70	183.9	59.54	41.45	33.18	30.12	26.46	25.27	24.61
0.80	193.8	60.39	41.33	32.64	29.31	25.53	24.24	23.43
0.90	204.1	61.70	41.61	32.50	28.95	25.03	23.62	22.73
1.00	215.3	63.43	42.12	32.63	28.87	24.83	23.31	22.32
2.00	331.5	86.40	53.87	39.53	33.61	28.02	25.67	24.00
3.00	451.7	112.10	68.31	49.10	40.96	33.67	30.53	28.27
4.00	570.9	138.70	83.31	59.05	48.86	39.84	35.87	33.10
5.00	692.0	165.20	98.62	69.35	56.94	46.24	41.48	38.09
6.00	812.4	191.20	113.70	79.58	65.15	52.71	47.09	43.17
7.00	925.7	217.70	129.20	89.98	73.29	59.20	52.86	48.30
8.00	1051.0	244.70	144.70	100.60	81.42	65.69	58.58	53.48
9.00	1182.0	271.20	160.20	111.10	89.71	72.31	64.33	58.61
10.00	1291.0	297.90	175.30	121.00	98.00	78.80	70.09	63.85

TABLE X. Upper limits for production cross section in fb for the VTDM model.

Tau (ns)	Mass (GeV)							
	91	200	300	400	500	600	700	800
0.01	968.4	10390	63800	318700	1.44×10^6	4.17×10^6	2.08×10^7	1.993×10^9
0.02	187.4	753.3	2580	6434	15530	31210	64850	1.272×10^5
0.03	99.06	256.7	649.0	1246	2324	3940	7094	11360
0.04	70.91	142.5	293.7	482.5	768.2	1179	1909	2814
0.05	58.26	97.35	173.7	259.1	377.6	538	797.9	1107
0.06	51.03	74.99	120.8	167.5	227.3	305.9	427.8	568.8
0.07	46.74	61.99	91.81	120.3	155.8	200.1	267.2	346.2
0.08	43.78	53.73	74.67	93.6	115.7	144.3	185.5	234.1
0.09	42.08	48.14	63.26	76.32	91.49	110.7	137.8	171.0
0.10	40.82	44.04	55.33	64.85	75.57	89.13	108.5	131.5
0.20	39.73	31.48	31.05	30.94	31.24	32.42	34.65	38.01
0.30	44.16	30.43	27.20	25.28	24.10	23.72	24.04	25.21
0.40	49.87	31.55	26.64	23.81	21.96	21.04	20.65	21.10
0.50	55.79	33.48	27.21	23.70	21.43	20.07	19.35	19.46
0.60	62.01	35.80	28.28	24.20	21.52	19.89	18.90	18.79
0.70	68.19	38.24	29.61	24.99	21.96	20.08	18.89	18.63
0.80	74.55	40.82	31.07	25.93	22.60	20.47	19.12	18.72
0.90	80.84	43.43	32.66	27.04	23.36	21.04	19.51	18.99
1.00	87.22	46.19	34.35	28.19	24.18	21.68	20.00	19.39
2.00	151.5	74.27	52.21	41.35	34.33	29.92	26.88	25.45
3.00	214.7	102.9	70.72	55.27	45.31	38.97	34.71	32.56
4.00	278.2	131.0	89.24	69.35	56.41	48.31	42.70	39.88
5.00	342.8	159.6	108.3	83.51	67.45	57.69	50.81	47.35
6.00	405.8	188.5	127.1	97.46	78.65	66.98	58.93	54.77
7.00	470.1	215.9	145.6	111.7	89.95	76.58	67.03	62.31
8.00	534.0	245.8	164.0	126.1	101.00	85.79	75.19	69.79
9.00	596.9	273.2	182.9	139.7	112.50	95.21	83.59	77.21
10.00	662.8	303.2	201.7	154.7	123.40	104.40	91.62	84.86

[1] G. Bertone, D. Hooper, and J. Silk, Phys. Rep. **405**, 279 (2005).
[2] A. Boveia and C. Doglioni, Annu. Rev. Nucl. Part. Sci. **68**, 429 (2018).
[3] P. Schwaller and J. Zurita, J. High Energy Phys. 03 (2014) 060.
[4] D. Barducci, A. Belyaev, A. K. M. Bharucha, W. Porod, and V. Sanz, J. High Energy Phys. 07 (2015) 066.
[5] The ATLAS Collaboration, Report No. ATL-PHYS-PUB-2018-048, 2018.
[6] CMS Collaboration, Report No. CMS-PAS-FTR-18-001, 2018.
[7] M. Cirelli, N. Fornengo, and A. Strumia, Nucl. Phys. **B753**, 178 (2006).
[8] A. Belyaev, G. Cacciapaglia, I. P. Ivanov, F. Rojas-Abatte, and M. Thomas, Phys. Rev. D **97**, 035011 (2018).
[9] D. Curtin *et al.*, Rep. Prog. Phys. **82**, 116201 (2019).
[10] J. Alimena *et al.*, J. Phys. G **47**, 090501 (2020).
[11] The ATLAS Collaboration, Report No. ATL-PHYS-PUB-2019-011, 2019.
[12] D. Curtin, K. Deshpande, O. Fischer, and J. Zurita, J. High Energy Phys. 07 (2018) 024.
[13] M. Aaboud *et al.* (ATLAS Collaboration), J. High Energy Phys. 06 (2018) 022.
[14] A. M. Sirunyan *et al.* (CMS Collaboration), Phys. Lett. B **806**, 135502 (2020).
[15] R. Mahbubani, P. Schwaller, and J. Zurita, J. High Energy Phys. 06 (2017) 119.
[16] H. Fukuda, N. Nagata, H. Otono, and S. Shirai, Phys. Lett. B **781**, 306 (2018).
[17] M. Saito, R. Sawada, K. Terashi, and S. Asai, Eur. Phys. J. C **79**, 469 (2019).
[18] J.-W. Wang, X.-J. Bi, Q.-F. Xiang, P.-F. Yin, and Z.-H. Yu, Phys. Rev. D **97**, 035021 (2018).
[19] A. Bharucha, F. Brümmer, and N. Desai, J. High Energy Phys. 11 (2018) 195.
[20] L. Calibbi, L. Lopez-Honorez, S. Lowette, and A. Mariotti, J. High Energy Phys. 09 (2018) 037.
[21] A. Biswas, D. Borah, and D. Nanda, J. Cosmol. Astropart. Phys. 09 (2018) 014.
[22] Q.-H. Cao, T. Gong, K.-P. Xie, and Z. Zhang, Sci. China Phys. Mech. Astron. **62**, 981011 (2019).
[23] D. Borah, D. Nanda, N. Narendra, and N. Sahu, Nucl. Phys. **B950**, 114841 (2020).
[24] G. Belanger *et al.*, J. High Energy Phys. 02 (2019) 186.
[25] A. Filimonova and S. Westhoff, J. High Energy Phys. 02 (2019) 140.
[26] A. Biswas, D. Borah, and D. Nanda, J. High Energy Phys. 12 (2019) 109.
[27] S. Jana, N. Okada, and D. Raut, J. High Energy Phys. 01 (2021) 198.
[28] C.-W. Chiang, G. Cottin, Y. Du, and M. J. Ramsey-Musolf, J. High Energy Phys. 01 (2021) 198.
[29] G. Cottin, N. Desai, S. Kraml, and A. Lessa, LLP Recasting Repository, https://github.com/llprecasting/recastingCodes/ (2019).
[30] A. Lahanas, K. Tamvakis, and N. Tracas, Phys. Lett. B **324**, 387 (1994).
[31] D. Pierce and A. Papadopoulos, Nucl. Phys. **B430**, 278 (1994).
[32] D. M. Pierce, J. A. Bagger, K. T. Matchev, and R.-j. Zhang, Nucl. Phys. **B491**, 3 (1997).
[33] M. Drees, M. M. Nojiri, D. Roy, and Y. Yamada, Phys. Rev. D **56**, 276 (1997); **64**, 039901(E) (2001).
[34] T. Fritzsche and W. Hollik, Eur. Phys. J. C **24**, 619 (2002).
[35] S. P. Martin, Phys. Rev. D **72**, 096008 (2005).
[36] Y. Yamada, Phys. Lett. B **682**, 435 (2010).
[37] E. Aprile *et al.* (XENON Collaboration), Phys. Rev. Lett. **121**, 111302 (2018).
[38] N. G. Deshpande and E. Ma, Phys. Rev. D **18**, 2574 (1978).
[39] E. Ma, Phys. Rev. D **73**, 077301 (2006).
[40] R. Barbieri, L. J. Hall, and V. S. Rychkov, Phys. Rev. D **74**, 015007 (2006).
[41] L. Lopez Honorez, E. Nezri, J. F. Oliver, and M. H. Tytgat, J. Cosmol. Astropart. Phys. 02 (2007) 028.
[42] A. S. Belyaev, A. Freegard, I. F. Ginzburg, T. Hosken, D. Locke, and A. Pukhov (to be published).
[43] A. Belyaev, G. Cacciapaglia, J. Mckay, D. Marin, and A. R. Zerwekh, Phys. Rev. D **99**, 115003 (2019).
[44] C. Arina, F.-S. Ling, and M. H. G. Tytgat, J. Cosmol. Astropart. Phys. 10 (2009) 018.
[45] E. Nezri, M. H. G. Tytgat, and G. Vertongen, J. Cosmol. Astropart. Phys. 04 (2009) 014.
[46] X. Miao, S. Su, and B. Thomas, Phys. Rev. D **82**, 035009 (2010).
[47] M. Gustafsson, S. Rydbeck, L. Lopez-Honorez, and E. Lundstrom, Phys. Rev. D **86**, 075019 (2012).
[48] A. Arhrib, R. Benbrik, and N. Gaur, Phys. Rev. D **85**, 095021 (2012).
[49] B. Swiezewska and M. Krawczyk, Phys. Rev. D **88**, 035019 (2013).
[50] A. Goudelis, B. Herrmann, and O. Stal, J. Cosmol. Astropart. Phys. 09 (2013) 106.
[51] A. Arhrib, Y.-L. S. Tsai, Q. Yuan, and T.-C. Yuan, J. Cosmol. Astropart. Phys. 06 (2014) 030.
[52] M. Krawczyk, D. Sokolowska, P. Swaczyna, and B. Swiezewska, J. High Energy Phys. 09 (2013) 055.
[53] M. Krawczyk, D. Sokolowska, P. Swaczyna, and B. Swiezewska, Acta Phys. Pol. B **44**, 2163 (2013).
[54] A. Ilnicka, M. Krawczyk, and T. Robens, Phys. Rev. D **93**, 055026 (2016).
[55] M. A. Díaz, B. Koch, and S. Urrutia-Quiroga, Adv. High Energy Phys. **2016**, 1 (2016).
[56] K. P. Modak and D. Majumdar, Astrophys. J. Suppl. **219**, 37 (2015).
[57] F. S. Queiroz and C. E. Yaguna, J. Cosmol. Astropart. Phys. 02 (2016) 038.
[58] C. Garcia-Cely, M. Gustafsson, and A. Ibarra, J. Cosmol. Astropart. Phys. 02 (2016) 043.
[59] M. Hashemi and S. Najjari, Eur. Phys. J. C **77**, 592 (2017).
[60] P. Poulose, S. Sahoo, and K. Sridhar, Phys. Lett. B **765**, 300 (2017).
[61] A. Alves, D. A. Camargo, A. G. Dias, R. Longas, C. C. Nishi, and F. S. Queiroz, J. High Energy Phys. 10 (2016) 015.
[62] A. Datta, N. Ganguly, N. Khan, and S. Rakshit, Phys. Rev. D **95**, 015017 (2017).
[63] N. G. Deshpande and E. Ma, Phys. Rev. D **18**, 2574 (1978).

[64] R. Barbieri, L. J. Hall, and V. S. Rychkov, Phys. Rev. D **74**, 015007 (2006).
[65] I. F. Ginzburg, K. A. Kanishev, M. Krawczyk, and D. Sokolowska, Phys. Rev. D **82**, 123533 (2010).
[66] M. Gustafsson, S. Rydbeck, L. Lopez-Honorez, and E. Lundstrom, Phys. Rev. D **86**, 075019 (2012).
[67] R. Mahbubani and L. Senatore, Phys. Rev. D **73**, 043510 (2006).
[68] R. Enberg, P. J. Fox, L. J. Hall, A. Y. Papaioannou, and M. Papucci, J. High Energy Phys. 11 (2007) 014.
[69] T. Cohen, J. Kearney, A. Pierce, and D. Tucker-Smith, Phys. Rev. D **85**, 075003 (2012).
[70] L. Lopez Honorez, M. H. G. Tytgat, P. Tziveloglou, and B. Zaldivar, J. High Energy Phys. 04 (2018) 011.
[71] Search for direct pair production of higgsinos by the reinterpretation of the disappearing track analysis with 36.1 fb^{-1} of $\sqrt{s} = 13$ TeV data collected with the ATLAS experiment, Technical Report No. ATL-PHYS-PUB-2017-019, CERN, Geneva, 2017.
[72] P. A. R. Ade *et al.* (Planck Collaboration), Astron. Astrophys. **594**, A13 (2016).
[73] A. Belyaev, N. D. Christensen, and A. Pukhov, Comput. Phys. Commun. **184**, 1729 (2013).
[74] A. V. Semenov, arXiv:hep-ph/9608488.
[75] A. V. Semenov, Nucl. Instrum. Methods Phys. Res., Sect. A **389**, 293 (1997).
[76] A. Semenov, Comput. Phys. Commun. **180**, 431 (2009).
[77] M. Bondarenko, A. Belyaev, L. Basso, E. Boos, V. Bunichev *et al.*, arXiv:1203.1488.
[78] Search for long-lived charginos based on a disappearing-track signature in pp collisions at $\sqrt{s} = 13$ TeV with the ATLAS detector, 2018.
[79] G. F. Giudice, M. A. Luty, H. Murayama, and R. Rattazzi, J. High Energy Phys. 12 (1998) 027.
[80] L. Randall and R. Sundrum, Nucl. Phys. **B557**, 79 (1999).
[81] T. Sjöstrand, S. Ask, J. R. Christiansen, R. Corke, N. Desai, P. Ilten, S. Mrenna, S. Prestel, C. O. Rasmussen, and P. Z. Skands, Comput. Phys. Commun. **191**, 159 (2015).
[82] J. de Favereau *et al.* (DELPHES 3 Collaboration), J. High Energy Phys. 02 (2014) 057.
[83] R. D. Ball *et al.* (NNPDF Collaboration), J. High Energy Phys. 04 (2015) 040.
[84] W. Beenakker, R. Hopker, and M. Spira, arXiv:hep-ph/9611232.
[85] W. Abdallah *et al.* (LHC Reinterpretation Forum), SciPost Phys. **9**, 022 (2020).
[86] G. Aad *et al.* (ATLAS Collaboration), Eur. Phys. J. C **70**, 787 (2010).
[87] L. Lonnblad and S. Prestel, J. High Energy Phys. 03 (2012) 019.
[88] A. Schalicke and F. Krauss, J. High Energy Phys. 07 (2005) 018.
[89] S. Hoeche, F. Krauss, S. Schumann, and F. Siegert, J. High Energy Phys. 05 (2009) 053.
[90] N. Fischer and S. Prestel, Eur. Phys. J. C **77**, 601 (2017).
[91] L. Lonnblad, J. High Energy Phys. 05 (2002) 046.
[92] S. Catani, F. Krauss, R. Kuhn, and B. R. Webber, J. High Energy Phys. 11 (2001) 063.
[93] J. Alwall *et al.*, Eur. Phys. J. C **53**, 473 (2008).
[94] M. L. Mangano, M. Moretti, and R. Pittau, Nucl. Phys. **B632**, 343 (2002).
[95] B. Cooper, J. Katzy, M. L. Mangano, A. Messina, L. Mijovic, and P. Skands, Eur. Phys. J. C **72**, 2078 (2012).
[96] J. R. Christiansen and S. Prestel, Eur. Phys. J. C **76**, 39 (2016).
[97] H. Dreiner, M. Kraemer, and J. Tattersall, Phys. Rev. D **87**, 035006 (2013).
[98] M. Ibe, S. Matsumoto, and R. Sato, Phys. Lett. B **721**, 252 (2013).
[99] A. Heister *et al.* (ALEPH Collaboration), Phys. Lett. B **533**, 223 (2002).
[100] G. Abbiendi *et al.* (OPAL Collaboration), Eur. Phys. J. C **26**, 479 (2003).
[101] G. Abbiendi *et al.* (OPAL Collaboration), Phys. Lett. B **572**, 8 (2003).
[102] J. Abdallah *et al.* (DELPHI Collaboration), Eur. Phys. J. C **31**, 421 (2003).
[103] V. Khachatryan *et al.* (CMS Collaboration), Report No. CMS-PAS-EXO-16-036, 2016, http://cds.cern.ch/record/2205281.
[104] M. Aaboud *et al.* (ATLAS Collaboration), Phys. Lett. B **788**, 96 (2019).
[105] M. Aaboud *et al.* (ATLAS Collaboration), J. High Energy Phys. 01 (2018) 126.
[106] A. Belyaev, S. Moretti, T. R. Fernandez Perez Tomei, S. F. Novaes, P. G. Mercadante, C. S. Moon, L. Panizzi, F. Rojas, and M. Thomas, Phys. Rev. D **99**, 015011 (2019).
[107] D. Dercks, N. Desai, J. S. Kim, K. Rolbiecki, J. Tattersall, and T. Weber, Comput. Phys. Commun. **221**, 383 (2017).
[108] Selection of jets produced in 13 TeV proton-proton collisions with the ATLAS detector, Technical Report No. ATLAS-CONF-2015-029, CERN, Geneva, 2015.
[109] Search for disappearing tracks in proton-proton collisions at $\sqrt{s} = 13$ TeV, Technical Report No. CMS-PAS-EXO-19-010, CERN, Geneva, 2020.
[110] Search for disappearing tracks in proton-proton collisions at $\sqrt{s} = 13$ TeV, 2020.